
Article:
Wrzosek-Lipska, K., Rezynkina, K., Bree, N. et al. (67 more authors) (2019) Electromagnetic properties of low-lying states in neutron-deficient Hg isotopes : Coulomb excitation of 182Hg, 184Hg, 186Hg and 188Hg. European Physical Journal A. 130. ISSN 1434-601X

https://doi.org/10.1140/epja/i2019-12815-2

Eur. Phys. J. A (2019) **55**: 130
DOI 10.1140/epja/i2019-12815-2

THE EUROPEAN PHYSICAL JOURNAL A

Regular Article – Experimental Physics

Electromagnetic properties of low-lying states in neutron-deficient Hg isotopes: Coulomb excitation of ^{182}Hg, ^{184}Hg, ^{186}Hg and ^{188}Hg

K. Wrzosek-Lipska[1,2,a], K. Rezynkina[2,3], N. Bree[2], M. Zielińska[1,4], L.P. Gaffney[5,2,6,7], A. Petts[5], A. Andreyev[2,8], B. Bastin[2,9], M. Bender[10], A. Blazhev[11], B. Bruyneel[11], P.A. Butler[5], M.P. Carpenter[12], J. Cederkäll[13,6], E. Clément[9,6], T.E. Cocolios[2,6,14], A.N. Deacon[14], J. Diriken[2,15], A. Ekström[13], C. Fitzpatrick[14], L.M. Fraile[16], Ch. Fransen[11], S.J. Freeman[14], J.E. García-Ramos[17], K. Geibel[11], R. Gernhäuser[18], T. Grahn[19,20], M. Guttormsen[21], B. Hadinia[7,22], K. Hadyńska-Klęk[1], M. Hass[23], P.-H. Heenen[24†], R.-D. Herzberg[5], H. Hess[11], K. Heyde[25], M. Huyse[2], O. Ivanov[2], D.G. Jenkins[8], R. Julin[19], N. Kesteloot[2,15], Th. Kröll[26], R. Krücken[18], A.C. Larsen[21], R. Lutter[27], P. Marley[8], P.J. Napiorkowski[1], R. Orlandi[2,7], R.D. Page[5], J. Pakarinen[19,20], N. Patronis[2,28], P.J. Peura[19], E. Piselli[6], L. Próchniak[1], P. Rahkila[19], E. Rapisarda[29,6], P. Reiter[11], A.P. Robinson[8,30], M. Scheck[5,7], S. Siem[21], K. Singh Chakkal[23], J.F. Smith[7], J. Srebrny[1], I. Stefanescu[2,18], G.M. Tveten[21], P. Van Duppen[2], J. Van de Walle[6], D. Voulot[6], N. Warr[11], A. Wiens[11], and J.L. Wood[31]

[1] Heavy Ion Laboratory, University of Warsaw, PL-02-093 Warsaw, Poland
[2] Instituut voor Kern- en Stralingsfysica, KU Leuven, BE-3001 Leuven, Belgium
[3] Université de Strasbourg, CNRS, IPHC UMR7178, F-67000 Strasbourg, France
[4] IRFU CEA, Université Paris-Saclay, F-91191 Gif-sur-Yvette, France
[5] Oliver Lodge Laboratory, University of Liverpool, Liverpool L69 7ZE, UK
[6] ISOLDE, CERN, CH-1211 Geneva 23, Switzerland
[7] School of Engineering, Computing and Physical Sciences, University of the West of Scotland, Paisley PA1 2BE, UK
[8] Department of Physics, University of York, York YO10 5DD, UK
[9] GANIL CEA/DSM-CNRS/IN2P3, Boulevard H. Becquerel, F-14076 Caen, France
[10] IPNL, Université de Lyon, Université Lyon 1, CNRS/IN2P3, F-69622 Villeurbanne Cedex, France
[11] Institut für Kernphysik, Universität zu Köln, DE-50937 Köln, Germany
[12] Physics Division, Argonne National Laboratory, Argonne, Illinois 60439, USA
[13] Physics Department, University of Lund, Box 118, SE-221 00 Lund, Sweden
[14] School of Physics and Astronomy, University of Manchester M13 9PL, Manchester UK
[15] Belgian Nuclear Research Centre SCK CEN, B-2400 Mol, Belgium
[16] Grupo de Física Nuclear, Universidad Complutense de Madrid, 28040 Madrid, Spain
[17] Departamento de Ciencias Integradas y Centro de Estudios Avanzados en Física, Matemáticas y Computación, Universidad de Huelva, 21071 Huelva, Spain
[18] Physics Department E12, Technische Universität München, D-85748 Garching, Germany
[19] University of Jyväskylä, Department of Physics, P.O. Box 35, FI-40014 University of Jyvaskyla, Finland
[20] Helsinki Institute of Physics, University of Helsinki, P.O. Box 64, FIN-00014 Helsinki, Finland
[21] Department of Physics, University of Oslo, N-0316 Oslo, Norway
[22] Department of Physics, University of Guelph, Guelph, Ontario N1G 2W1, Canada
[23] Department of Particle Physics, Weizmann Institute of Science, Rehovot 76100, Israel
[24] Physique Nucléaire Théorique, Université Libre de Bruxelles, B-1050 Bruxelles, Belgium
[25] Department of Physics and Astronomy, Ghent University, B-9000 Gent, Belgium
[26] Institut für Kernphysik, Technische Universität Darmstadt, D-64289 Darmstadt, Germany
[27] Department of Physics, Ludwig Maximilian Universität München, 85748 Garching, Germany
[28] Department of Physics, The University of Ioannina, GR-45110 Ioannina, Greece
[29] Paul Scherrer Institut, 5232 Villigen PSI Switzerland
[30] National Physical Laboratory, Hampton Road, Teddington TW11 0LW, UK
[31] School of Physics, Georgia Institute of Technology, Atlanta, Georgia 30332-0430, USA

Received: 27 February 2019 / Revised: 7 June 2019
Published online: 22 August 2019

Communicated by M.J. Garcia Borge

Abstract. The neutron-deficient mercury isotopes serve as a classical example of shape coexistence, whereby at low energy near-degenerate nuclear states characterized by different shapes appear. The electromagnetic structure of even-mass $^{182-188}$Hg isotopes was studied using safe-energy Coulomb excitation of neutron-deficient mercury beams delivered by the REX-ISOLDE facility at CERN. The population of $0^+_{1,2}$, $2^+_{1,2}$ and 4^+_1 states was observed in all nuclei under study. Reduced $E2$ matrix elements coupling populated yrast and non-yrast states were extracted, including their relative signs. These are a sensitive probe of shape coexistence and may be used to validate nuclear models. The experimental results are discussed in terms of mixing of two different configurations and are compared with three different model calculations: the Beyond Mean Field model, the Interacting Boson Model with configuration mixing and the General Bohr Hamiltonian. Partial agreement with experiment was observed, hinting to missing ingredients in the theoretical descriptions.

1 Introduction

The neutron-deficient mercury isotopes ($Z = 80$) serve as an illustrative example of shape coexistence [1,2], whereby at low excitation energies near-degenerate nuclear states are characterized by different shapes. The first observation of a dramatic change in the ground-state mean-square charge radii was observed through isotope shift measurements in ^{183}Hg and ^{185}Hg, when comparing to heavier-mass mercury isotopes [3]. Since then a large amount of information has been collected for nuclei around the $N = 104$ midshell between $N = 82$ and $N = 126$ using different experimental techniques. This resulted, amongst others, in the observation of a large odd-even staggering in the isotope shifts in the mercury isotopes around $^{181-185}$Hg [4], which has long been attributed to the intruder structure becoming the ground state in the odd-mass isotopes and the observation of shape coexistence at low excitation energy in ^{185}Hg [5]. Recent results obtained from isotope-shift measurements extended the knowledge on the ground-state deformation systematics down to ^{177}Hg [6]. Further, lifetime measurements performed for ^{184}Hg and ^{186}Hg [7,8] suggested a sudden increase in deformation of the excited yrast states with the spin larger than two. Radioactive-decay studies identified coexisting bands in ^{184,186,188}Hg, assumed to be characterized by different deformations [9–11]. This phenomenon was observed in ^{182}Hg as well by means of in-beam spectroscopy studies [12].

The energy-level systematics of the even-even mercury isotopes ranging from $A = 190$ to $A = 198$ reveals a nearly constant excitation energy of the yrast states up to the spin $I = 6$ [13, 14]. Mean-field calculations interpret these states as exhibiting a weakly-deformed oblate character [1, 15, 16]. However, this regular pattern is distorted for the lighter mercury isotopes ($N \leq 106$) through the intrusion of levels of a very collective rotational band of assumed prolate nature, which decreases in excitation energy reaching a minimum around mass $A = 182, 184$ [13, 14]. In a shell-model picture, the energy evolution of the deformed states as a function of neutron number can be interpreted as arising from a proton pair excitation across the $Z = 82$ shell closure. This leads to extra valence proton pairs interacting with the valence neutrons through the attractive quadrupole proton-neutron interaction [1]. By contrast, in a mean-field picture the difference in excitation energy between the oblate and prolate states results from the variation of the density of single-particle levels around the Fermi energy with deformation in the Nilsson diagram.

The energy of the 2^+_1 state, as well as the $B(E2; 2^+_1 \rightarrow 0^+_1)$ value in even-even mercury isotopes around $N = 104$ are relatively constant, which is commonly interpreted as a manifestation of a similar structure of these states. On the other hand, large conversion coefficients related to the substantial $E0$ components in the $2^+_2 \rightarrow 2^+_1$ transition, observed for ^{182,184,186}Hg [17, 18], indicate a large degree of mixing. Indeed, as it was reported in ref. [19], the composition of the 2^+ state changes significantly in the light mercury isotopes, which is reflected in large variations of mixing amplitudes extracted using the Variable Moment of Inertia (VMI) model. We performed Coulomb-excitation (Coulex) studies using post-accelerated mercury beams and deduced $E2$ matrix elements between yrast and non-yrast states [20]. The results were interpreted within the two-state mixing model supporting the mixing of a weakly-deformed oblate-like structure with a more-deformed prolate-like structure.

In this paper we present the experimental details and the analysis procedure of the Coulomb-excitation studies of ^{182,184,186,188}Hg reported in ref. [20]. However, it should be noted that the results for ^{182,184}Hg reported in ref. [20] have been extracted using preliminary values of a number of γ-ray branching ratios and conversion coefficients determined in a β-decay study of ^{182,184}Tl populating excited states in ^{182,184}Hg. Some of these originaly used spectroscopic data, particularly total conversion coefficients $\alpha(2^+_2 \rightarrow 2^+_1)$ in ^{182,184}Hg, turned out be erroneous and they were corrected in the subsequent, complete analysis of the same β-decay data set and published in ref. [17]. In the current paper, we performed a full re-analysis of the Coulomb-excitation data for ^{182,184}Hg using the corrected values of those spectroscopic data [17] which substantially differ from the preliminary values assumed in ref. [20]. Consequently, for these two nuclei, the data reported in the present paper replace the results from ref. [20].

[a] e-mail: wrzosek@slcj.uw.edu.pl
[†] Deceased.

The experimental technique, the production and post-acceleration of mercury beams at REX-ISOLDE are presented in sect. 2. The data analysis and the extraction of the reduced matrix elements are presented in sects. 3, 4 and in sect. 5, respectively. A comparison of experimental excitation energies and quadrupole moments with theoretical predictions based on three different models (the quadrupole collective General Bohr Hamiltonian model (GBH) [21], the interacting boson model with configuration mixing (IBM-CM) [22] and the beyond-mean-field model (BMF) [16]) is given in sect. 6. The experimental and theoretical monopole transition strengths, $\rho^2(E0; 2_2^+ \rightarrow 2_1^+)$, are discussed in sect. 7. A summary and outlook are given in sect. 8.

2 Measurements

2.1 Production and postacceleration of exotic, neutron-deficient mercury beams

The neutron-deficient mercury isotopes were produced through the spallation reaction induced by a 1.4 GeV proton beam, delivered from the Proton Synchrotron Booster at CERN, impinging on a molten lead target. The resulting products rapidly diffused out of the target, which was heated up to 600 °C, passed through the transfer line, and were ionized in a high-temperature plasma ion source. The 1^+ ions were extracted from the ion source by applying a 30.2 kV electrostatic potential and were, subsequently, mass-separated by the General Purpose Separator (GPS). Possible beam contaminations from lead and gold isotopes were negligible since the temperature of the target container and the transfer line was kept around 600 °C: the vapor pressure of mercury (*i.e.*, its evaporation rate out of the target container) is four orders of magnitude higher than that of lead, and twelve orders of magnitude higher than that of gold at this temperature.

The low-energetic singly-charged radioactive ion beam was then guided to the REX postaccelerator. The ions were injected into the REX Penning trap (REXTRAP) to cool and bunch the beam. The bunches were transmitted to the Electron Beam Ion Source (REXEBIS) afterwards, where they were brought to a higher charge state. The final charge states of the studied mercury isotopes are listed in table 1. In the experiment performed in 2007, the charge breeding time in EBIS was equal to 170 ms. This time is identical to the trapping time in REXTRAP. In consequence EBIS bunches the ions into the REX post-accelerator at a rate of ~ 6 Hz. In 2008, the EBIS breeding time was set to 200 ms, corresponding to a bunching frequency of 5 Hz. In order to avoid additional stable beam contaminants in the radioactive ion beam (originating from *e.g.*, the REXTRAP buffer gas and residual gases inside REXEBIS), the ions were separated according to their A/q ratio prior to injection in the REX linear accelerator (REX-LINAC) [23]. The highly-charged radioactive mercury ions were post-accelerated at the REX-LINAC to an energy of 2.85 MeV/A.

2.2 Coulomb excitation of $^{182-188}$Hg

The post-accelerated radioactive mercury beams were delivered to the Miniball set-up [24]. Coulomb excitation of ^{182,184,186,188}Hg was induced by ^{120}Sn, ^{107}Ag, and ^{112,114}Cd secondary targets with thicknesses of 2.3, 1.1, and 2 mg/cm^2, respectively. The γ rays depopulating Coulomb-excited states in the ejectile and target nuclei were detected with the Miniball γ-ray spectrometer, which consists of eight clusters. Each of these clusters contains three HPGe crystals, which are electrically divided into six segments and a central electrode. During the experimental campaigns performed in 2007 and 2008, 23 and 18 out of 24 crystals were operational, respectively. To determine the full-energy γ-ray efficiency of the Miniball array over the range corresponding to observed γ-ray transitions in mercury isotopes, down to the Hg K_α X-ray region ($K_{\alpha_1} = 70.8$ keV and $K_{\alpha_2} = 68.9$ keV), ^{133}Ba and ^{152}Eu calibration sources were used. The absolute γ-ray efficiency of Miniball was 6.80(18)% and 5.30(14)% at 1.3 MeV in 2007 and 2008, respectively. The energies of scattered target recoils and mercury ejectiles were measured with a double-sided silicon strip detector (DSSSD) [25], placed inside the compact collision chamber at a distance of 32.5 mm behind the cadmium target and 33.5 mm behind the tin and silver targets. The angular range covered by the DSSSD in the laboratory frame measured with respect to the beam direction extended from 15.5° to 51.6° (for measurements performed with the cadmium targets) and from 15° to 50.7° (for measurements performed with the tin and silver targets), corresponding to the center-of-mass angular ranges for projectile and target shown in table 1. The DSSSD is subdivided into four quadrants with 16 annular and 12 radial strips per quadrant, which allowed for a measurement of the angular distribution of both mercury ejectiles and target recoils. Based on the different kinematics and requesting two particles to be present in each event (see sect. 3 B), the detected recoils and ejectiles were identified in the DSSSD.

The detected γ rays were emitted in flight causing a Doppler shift in their detected energy. This is due to the fact that: (i) the lifetimes of the excited nuclear states of the investigated mercury isotopes are typically several picoseconds, while the time of flight of the projectile or recoil particles from the target to the DSSSD is in the range of a few nanoseconds, and (ii) the target thicknesses used in the measurements were smaller than the range of the particles in the target. The angular segmentation of the DSSSD and Miniball detection set-ups was essential to perform a reliable, event-by-event Doppler correction of the γ-ray energy.

The beam energies were chosen such that the distance between collision partners was greater than $1.25(A_P^{1/3} + A_T^{1/3}) + 5$ [fm] over the angular range covered by the DSSSD. This empirical condition, known as Cline's safe energy criterion [26], ensured purely electromagnetic interaction in the Coulomb-excitation process. For example, the "safe" energy for ^{184}Hg impinging on ^{112}Cd is equal to 807 MeV for the highest center-of-mass angle of 169.8°.

Table 1. Experimental parameters of the measurements. The first four columns give the isotope of interest, its half-life, $T_{1/2}$, the year of the experimental campaign and the selected charge state(s) for each mercury isotope. For each experiment the beam intensity, I_{Hg}, measured at the secondary target, the beam energy, E_{Hg}, the center-of-mass angular range, θ_{CM}, corresponding to angular range covered by the DSSSD in the laboratory frame for different projectile and target nuclei are listed. These angular ranges correspond to one- and two-particle detection ranges (see text for details). The total measurement time, t_{exp}, is given in the last column.

Isotope	$T_{1/2}$ [s]	Year	Charge	I_{Hg} [pps]	E_{Hg} [MeV]	Target(s)	θ_{CM}	t_{exp} [h]
^{182}Hg	10.8	2008	44^+	3.5×10^3	519	^{112}Cd	41.3°–169.8°	110.5
^{184}Hg	30.6	2007	43^+	4.8×10^3	524	^{120}Sn	38.4°–171.6°	58.7
						^{107}Ag	41.5°–168.6°	18.3
		2008	44^+	2.2×10^4		^{112}Cd	41.6°–169.5°	12.8
^{186}Hg	84	2007	43^+	2.1×10^5	530	^{120}Sn	38.7°–171.3°	3.0
						^{107}Ag	41.8°–168.3°	1.4
		2008	44^+	3.0×10^4		^{114}Cd	41.4°–169.6°	5.8
^{188}Hg	195	2007	44^+	1.6×10^5	536	^{120}Sn	39.0°–171.1°	11.4
						^{107}Ag	42.1°–167.9°	1.6
		2008	45^+	1.0×10^5		^{114}Cd	41.7°–169.3°	15.9

3 Data selection

3.1 Timing conditions

Beams delivered by the REX-ISOLDE facility have specific timing properties which influences the way data are taken at Miniball. The beam delivered to the REX-LINAC is bunched. Triggered by the EBIS signal, the REX-LINAC is switched on for 800 μs. During this active time window the Miniball data acquisition system registers all the information from the γ-ray and particle detectors. The detected "in-beam" γ-ray spectra contain not only the *prompt* radiation following Coulomb excitation, but also γ rays originating from β-decay, natural background radiation and X rays from the accelerator cavities. They all contribute to the observed γ-ray background (*random* γ rays), while the particle background mostly originates from the elastic Rutherford scattering process. The un-conditioned in-beam γ-ray spectrum obtained during the ^{184}Hg-on-^{112}Cd experiment is presented in fig. 1(a). Coincidences between a particle and a γ ray are crucial to distinguish the Coulomb-excitation events from the background radiation. In order to select the Coulomb-excitation events, each γ ray arising directly from the collision was correlated to one or more coincident ejectile/recoil particles. The time difference between the detected γ rays and the particles in a time window of 4 μs in the experiment of ^{184}Hg on the ^{112}Cd target is shown in fig. 1(d). A time window of 300 ns width was defined to select the *prompt* particle-γ events. Random particle-γ coincidences, indicated in green in fig. 1(d), were attributed to the un-correlated particle-γ events. In order to subtract the random γ-ray spectrum from the prompt one, the former was scaled by the ratio of the widths of the respective time windows. The resulting scaled random γ-ray spectrum for ^{184}Hg is presented in fig. 1(b) in green. After this procedure only the transitions resulting from Coulomb excitation remain, as shown in fig. 1(c). The Doppler-broadened photopeaks of γ rays originating from the $2_1^+ \rightarrow 0_1^+$, $4_1^+ \rightarrow 2_1^+$, $2_2^+ \rightarrow 0_1^+$ transitions in ^{184}Hg as well as the $2_1^+ \rightarrow 0_1^+$ transition in ^{112}Cd can be observed. A peak around 69 keV remains present, suggesting a production of X rays directly related

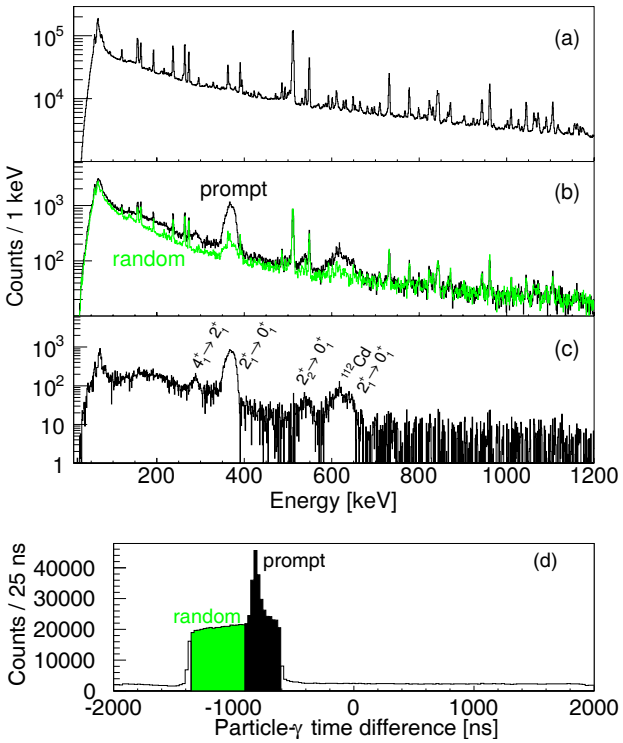

Fig. 1. (Color online) Gamma-ray spectra from the ^{184}Hg-on-^{112}Cd experiment illustrating the data processing: (a) In-beam, un-conditioned γ-ray spectrum detected in the Miniball array during the EBIS pulse; (b) Gamma-ray spectrum collected in a prompt (black) and random (green) coincidence with detected ejectile/recoil particle(s) in the DSSSD; (c) Random-subtracted prompt γ-ray spectrum of ^{184}Hg. No Doppler-correction has been applied; (d) time difference between the detected γ ray and scattered particle with indicated prompt (black) and random (green) coincidence windows.

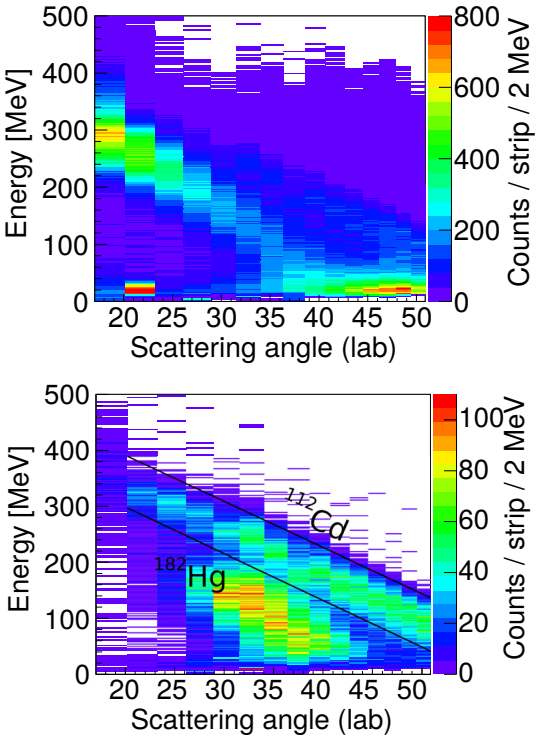

Fig. 2. (Color online). Particle energy *versus* scattering angle in the laboratory frame of reference for ^{182}Hg on ^{112}Cd. The color scale on the vertical axis represents the intensity in each bin. Top: unconditioned plot showing mainly elastically scattered particles in the DSSSD. Bottom: idem, but Coulomb-excitation events were selected by demanding the detection of exactly two particles in opposite quadrants of the DSSSD, being both in a prompt coincidence with each other and with a γ ray detected in Miniball.

to the collision. In the non-random-subtracted spectrum, a clear peak around 65 keV was present, arising mainly from the β^+/EC decay of ^{184}Ir on top of the X-ray radiation from the accelerator cavities. The X rays from both these sources are not time-correlated with the collision and thus are not present in the random-subtracted spectrum. The remaining X rays are related to the mercury beam. This issue will be discussed in more detail in sect. 4.

3.2 Two-particle event selection

In order to identify the scattered mercury beam and target ions, events were selected demanding detection of exactly two particles in opposite quadrants of the DSSSD in coincidence with a γ ray registered in Miniball. The centre-of-mass angular range, where two particles are incident on the DSSSD, is reduced as compared to the centre-of-mass angular range covered by the particle detector presented in table 1, and extends from 76.8° to 149° (for measurements performed with the cadmium targets) and from 78.6° to 150° (for measurements performed with the tin and silver targets). The events of interest were chosen by requesting the absolute time difference between the detection of two particles to be ≤ 50 ns. Figure 2 presents the number of counts corresponding to the detected ^{182}Hg-beam and ^{112}Cd-target ions as a function of the energy and scattering angle in the laboratory frame. It shows a typical inverse-kinematics scattering pattern. The heavier-mass beam particles are detected at smaller angles in the laboratory frame of reference, while the recoiling target nuclei are scattered throughout the whole detection range of the DSSSD. The separation between the ejectile and recoil ions is significantly improved when requesting detection of exactly two particles scattered back-to-back in the centre-of-mass frame (see bottom panel of fig. 2) compared to the spectrum obtained without this condition (top panel of fig. 2).

4 Data analysis

4.1 Mercury K X rays

In the background-subtracted γ-ray spectra intense $K_{\alpha,\beta}$ X ray peaks are observed for all studied isotopes at energy of 69 and 80 keV in addition to the γ rays following the Coulomb excitation of target and projectile. As it will be discussced in the following sections, origins of these mercury X rays include internal conversion of observed γ rays and $E0$ transitions. An additional source is related with the heavy-ion induced K-vacancy creation processes. The cross-section for the emission of a K_α X rays, originating from atomic processes, can be estimated from phenomenological approach, which gives the cross section as a function of beam energy, target proton number and ionization potential. Details of the method together with summary of all data concerning the observed X rays in Coulomb-excitation experiments on isotopes in the light-lead region at ISOLDE are given in ref. [27]. For the analysis of the mercury data the Coulomb excitation of ^{188}Hg were used to scale the theoretical predictions of the expected K X-ray yield from the K-vacancy creation process. The only states populated in the Coulomb excitation experiment of ^{188}Hg were 2_1^+ at 413 keV and 4_1^+ at 1005 keV (see sect. 4.5). As no low-lying excited 0^+ states or higher-lying 2^+ or 4^+ states, are observed in ^{188}Hg it was concluded that the only nuclear effect giving rise to mercury X rays, is internal conversion of observed γ ray transitions. After correcting for the latter, using known conversion coefficients [28], the remaining number of X rays was attributed to the heavy-ion induced K-vacancy creation process and used to rescale the calculated number of X rays predicted by theoretical formulas. A scaling factor of 0.037(5) results from a comparison of the number of observed and expected X rays. This factor is further useded to rescale the predicted amount of X rays originating from the heavy-ion induced K-vacancy creation process for lighter mercury isotopes. The contribution to the X-ray intensity from atomic effects observed in ^{182,184}Hg was deduced to be 13(3)% (for ^{182}Hg) and 14(4)% (for ^{184}Hg) of the total observed ones and the remaining excess of X rays indicate the presence of $E0$ deexcitations from the 0_2^+ and 2_2^+ states. The way how these two $E0$ transitions were distinguished using the $\gamma\gamma$ coincidences is presented in sects. 4.2 and 4.3.

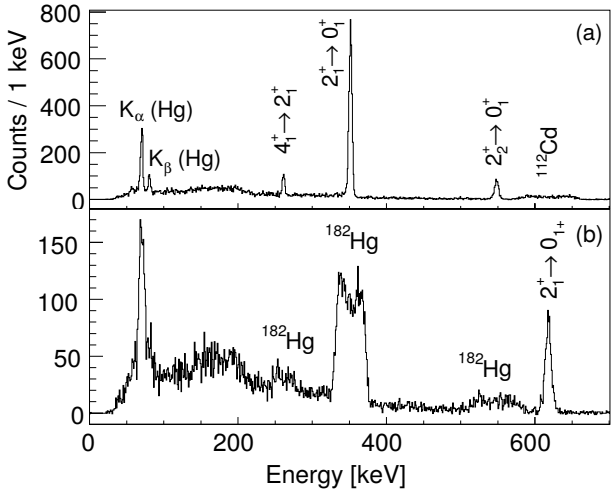

Fig. 3. Two-particle gated and random-subtracted γ-ray spectra ($2p - \gamma$). The spectrum (a) is Doppler-corrected assuming emission from the ^{182}Hg ejectile, whereas (b) is Doppler-corrected assuming emission from the ^{112}Cd recoil. The population of the 2_1^+ state in ^{112}Cd and of the 2_1^+, 2_2^+, 4_1^+ states in ^{182}Hg was observed. Intense K X-ray peaks are clearly visible in the spectrum (a) (see text for details). Figure 3(a) is adapted from ref. [20].

4.2 Experiment on ^{182}Hg

Coulomb excitation of ^{182}Hg ions was induced by a ^{112}Cd secondary target. Either the projectile or the target nucleus can be excited in a collision. The two-particle-gated γ-ray spectra, random-subtracted and Doppler-corrected for mass $A = 182$ and $A = 112$, are shown in fig. 3(a) and (b), respectively. In the latter, a clear peak at the energy of 617 keV is visible corresponding to the $2_1^+ \rightarrow 0_1^+$ γ-ray transition in ^{112}Cd. Sharp peaks at energies of 261 keV, 352 keV, 548 keV correspond to the $4_1^+ \rightarrow 2_1^+$, $2_1^+ \rightarrow 0_1^+$ and $2_2^+ \rightarrow 0_1^+$ γ-ray transitions in ^{182}Hg, respectively. Moreover, intense K_α (69 keV) and K_β (80 keV) X-ray peaks are clearly observed. The γ-ray and X-ray intensities are listed in table 2.

The observed K X rays are in prompt coincidence with two scattered particles and their Doppler correction is consistent with emission from the mercury projectile. As mentioned in sect. 4.1 they originate from:

1) the heavy-ion induced K-vacancy creation due to atomic processes taking place when the mercury beam passes through the target [27],
2) the internal conversion of the observed γ-ray transitions in ^{182}Hg,
3) the $E0$ de-excitation after Coulomb excitation.

Subtracting the number of X rays originating from the afore-mentioned first two sources, $7.2(6) \times 10^2$ counts corresponding to K_α X rays remains in ^{182}Hg. Those were attributed to the $E0$ de-excitation of the 0_2^+ and 2_2^+ states. Since the mixing ratio $\delta(\frac{E2}{M1})$ for the $2_2^+ \rightarrow 2_1^+$ transition is unknown in the investigated mercury isotopes, the value of 1.85 was adopted for the analysis (see sect. 5.1 for details).

Table 2. Measured γ-ray and K X-ray intensities (not efficiency corrected) for ^{182}Hg scattered on the ^{112}Cd target. The extracted intensities of the $E0$ $2_2^+ \rightarrow 2_1^+$ and $0_2^+ \rightarrow 0_1^+$ transitions, corrected for the K_α/K_β X-ray branching ratio and fluorescence effect, are also shown. The angular range for simultaneous detection of two particles is given in the centre-of-mass frame together with corresponding angular range for the target-nucleus (t) detection in laboratory frame. The intensities marked with asterisks were derived from the $\gamma\gamma$-coincidence analysis (as described in detail in the text).

Nucleus	$\Theta_{lab,t}$ ($\Theta_{c.m.}$)	Transition	Counts
^{182}Hg	18.7°–51.6°	$2_1^+ \rightarrow 0_1^+$	$3.81(7) \times 10^3$
	(76.8°–142.6°)	$2_2^+ \rightarrow 0_1^+$	$5.6(3) \times 10^2$
		$4_1^+ \rightarrow 2_1^+$	$3.2(4) \times 10^2$
		$2_2^+ \rightarrow 2_1^+$	$1.4(6) \times 10^{2*}$
		K_α (69 keV)	$1.02(5) \times 10^3$
		K_β (80 keV)	$2.9(4) \times 10^2$
		$2_2^+ \rightarrow 2_1^+$ $E0$	$2.9(9) \times 10^{2*}$
		$0_2^+ \rightarrow 0_1^+$	$6.9(13) \times 10^{2*}$
^{112}Cd		$2_1^+ \rightarrow 0_1^+$	$8.6(3) \times 10^2$

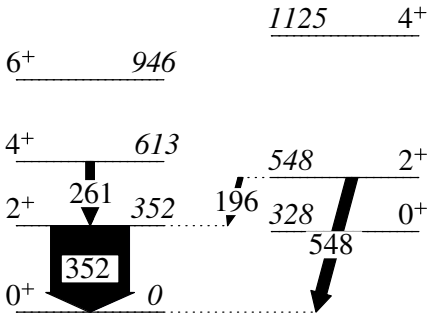

Fig. 4. Low-energy part of the level scheme of ^{182}Hg, relevant to the Coulomb-excitation analysis. Level and γ-ray transition energies are given in keV. Widths of the arrows are proportional to the measured γ-ray intensities. The intensities of the $0_2^+ \rightarrow 0_1^+$ and $2_2^+ \rightarrow 2_1^+$ $E0$ transitions, deduced from the analysis of the K X-ray peaks (see text for details) and given in table 2, were also included in the analysis. Figure adapted from ref. [20].

The low-energy level scheme of ^{182}Hg is presented in fig. 4, showing the γ-ray transitions that were observed, and the states included in the Coulomb-excitation analysis. Note that for all figures displaying level schemes, the levels are organized into yrast and non-yrast parts. No attempt has been made to assign levels to rotational bands of states of similar intrinsic structure. The reason for this choice is the high degree of mixing of the lowest energy states in the investigated mercury isotopes and the absence of a firm nuclear-model independent interpretation regarding the type of deformation for specific states (see sect. 6). The 196 keV $2_2^+ \rightarrow 2_1^+$ γ-ray transition is not visible in fig. 3(a) due to the presence of the Compton edge

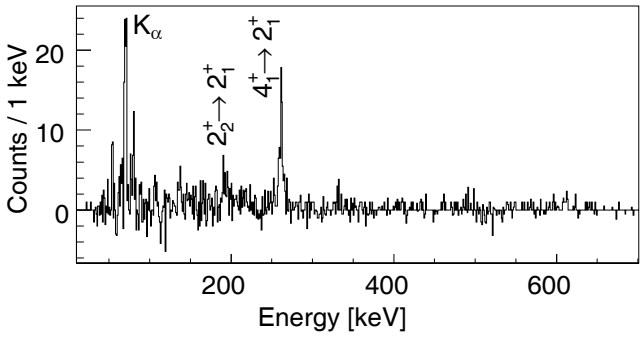

Fig. 5. Random-subtracted $\gamma\gamma$-coincidence spectrum gated on the $2_1^+ \rightarrow 0_1^+$ transition at the energy of 352 keV in ^{182}Hg, demanding that at least one particle satisfies the kinematic condition. The γ rays were Doppler corrected for the ^{182}Hg ejectile.

of the $2_1^+ \rightarrow 0_1^+$ transition at the energy of 204 keV. Consequently, the intensity of the $2_2^+ \rightarrow 2_1^+$ γ-ray transition was deduced from the $\gamma\gamma$-coincidence analysis.

The particle-gated $\gamma\gamma$ energy spectrum for ^{182}Hg is shown in fig. 5. Several γ-ray transitions, being in coincidence with the $2_1^+ \rightarrow 0_1^+$ γ ray, are visible in the spectrum: the $4_1^+ \rightarrow 2_1^+$ and $2_2^+ \rightarrow 2_1^+$ γ-ray transitions at energies of 261 keV and 196 keV, respectively, as well as K X rays. As the $4_1^+ \rightarrow 2_1^+$ transition is observed in both two-particle gated (*singles*) and particle-gated $\gamma\gamma$ (*coincidences*) spectra, the ratio of their intensities expressed as

$$R_{4_1^+ \rightarrow 2_1^+} = \frac{I_{coincidences}(4_1^+ \rightarrow 2_1^+)}{I_{singles}(4_1^+ \rightarrow 2_1^+)} \quad (1)$$

and equal to 0.26(5) can be used to extract the intensity of the $2_2^+ \rightarrow 2_1^+$ transition in singles. The result is given in table 2 and details of the procedure are provided in ref. [29].

Moreover, in the $\gamma\gamma$ coincidence spectrum K_α X rays are clearly visible. From the detected 74(15) counts of K_α X rays, 9(2) can be attributed to the K-vacancy creation due to atomic processes [27], *i.e.* process number 1. in the list given at the beginning of this section. The internal conversion of the observed $4_1^+ \rightarrow 2_1^+$ γ-ray transition in the coincidence spectrum is responsible for to 5(1) counts. After subtraction of these two sources of X rays 60(15) K_α X rays remain. As they are in coincidence with the $2_1^+ \rightarrow 0_1^+$ γ-ray transition, they can be attributed to the conversion of the $2_2^+ \rightarrow 2_1^+$ transition. Further, using the $R_{4_1^+ \rightarrow 2_1^+}$ scaling factor, the number of counts arising from this conversion in the two-particle gated γ-ray spectrum can be found to be equal to $2.3(7) \times 10^2$. Subtracting the latter from the total number of $7.2(6) \times 10^2$ K_α X rays, $4.9(9) \times 10^2$ counts remain. These were attributed to the $E0$ de-excitation of the 0_2^+ state. The final values were corrected for the K_α and K_β X-ray branching ratio equal to 3.6(1) [30], and the fluorescence effect [31]. The results are presented in table 2.

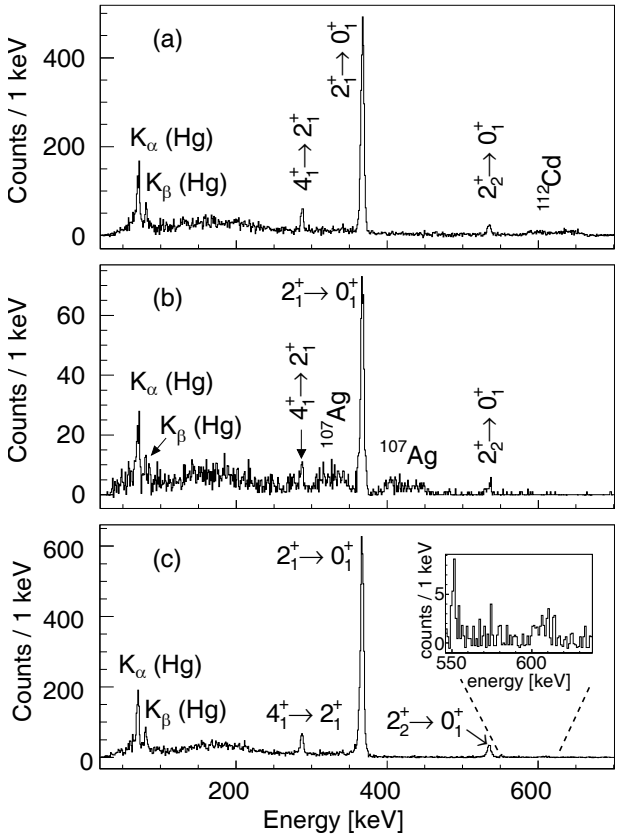

Fig. 6. Two-particle gated, random-subtracted and Doppler-corrected for the ^{184}Hg ejectile γ-ray spectrum following the Coulomb excitation of ^{184}Hg induced by three different targets: ^{112}Cd (a), ^{107}Ag (b) and ^{120}Sn (c). The population of the 2_1^+, 2_2^+, 4_1^+ states in ^{184}Hg is clearly visible, as well as intense K X-ray peaks. Additionally, in the experiment performed with the ^{120}Sn target, a weak $4_2^+ \rightarrow 2_2^+$ γ-ray transition (552 keV) and the $2_3^+ \rightarrow 0_2^+$ & $2_3^+ \rightarrow 2_1^+$ doublet (around 610 keV) in ^{184}Hg were observed. Figure 6(c) is adapted from ref. [2].

4.3 Experiment on ^{184}Hg

Coulomb excitation of ^{184}Hg was performed using three different secondary targets: ^{112}Cd, ^{107}Ag and ^{120}Sn. Two-particle-gated γ-ray spectra, random-subtracted and Doppler-corrected for the ejectile are presented in fig. 6. The population of the 2_1^+, 2_2^+ and 4_1^+ states in ^{184}Hg is clearly visible. Moreover, in the experiment with the ^{120}Sn target ($Z = 50$) the 4_2^+ and 2_3^+ states at 1086 keV and 983 keV, respectively, were excited, yielding the weak 552 keV $4_2^+ \rightarrow 2_2^+$ peak and a doublet of $2_3^+ \rightarrow 0_2^+$ and $2_3^+ \rightarrow 2_1^+$ γ-ray transitions. The low-energy level scheme of ^{184}Hg together with all observed γ-ray transitions in the Coulomb excitation experiment is shown in fig. 7. The extracted γ-ray and X-ray intensities are summarized in table 3.

Intense K_α X-ray peaks are clearly visible in the two-particle gated γ-ray spectra of ^{184}Hg. After subtracting those originating from the heavy-ion K-vacancy creation and from the internal conversion of the observed γ rays, a significant amount of $3.6(5) \times 10^2$ and $3.3(5) \times 10^2$ X rays

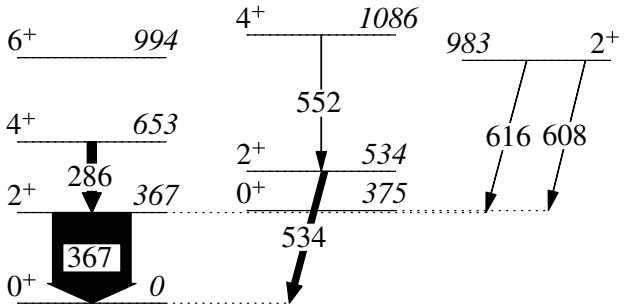

Fig. 7. Low-energy part of the level scheme of ^{184}Hg, relevant to the Coulomb-excitation analysis. Level and γ-ray transition energies are given in keV. Widths of the arrows are proportional to the measured γ-ray yields. As in the case of ^{182}Hg, the $0_2^+ \to 0_1^+$ and $2_2^+ \to 2_1^+$ $E0$ transitions were deduced from the analysis of the K X-ray peaks (see text for details). Figure adapted from ref. [20].

remains in the spectra of ^{184}Hg collected with the ^{112}Cd and ^{120}Sn targets, respectively. The $\gamma\gamma$ coincidence analysis, analogous to that performed for ^{182}Hg, allowed these X rays to be attributed to the $2_2^+ \to 2_1^+$ and $0_2^+ \to 0_1^+$ $E0$ transitions in ^{184}Hg. The low level of statistics collected in the experiment with the ^{107}Ag target does not allow such an analysis to be performed. As an example, the $\gamma\gamma$ coincidence spectrum, gated on the $2_1^+ \to 0_1^+$ γ-ray transition in ^{184}Hg, for the experiment performed with the ^{120}Sn target is shown in fig. 8. The 286 keV $4_1^+ \to 2_1^+$ γ-ray transition and the K_αX rays are clearly visible. After correcting for the internal conversion and the K_α-vacancy creation process, 55(17) K_αX rays remain. For the experiment performed with the ^{112}Cd target the number of K_αX rays deduced from the $\gamma\gamma$ coincidence analysis is equal to 29(20). In both cases these numbers were attributed to the $E0$ component of the $2_2^+ \to 2_1^+$ transition in ^{184}Hg. Further, following the method described in sect. 4.2, the intensity of the $E0$ transitions between the excited 2_2^+ and 2_1^+ states as well as between the excited 0_2^+ state and the 0_1^+ ground state can be deduced for the two-particle-gated γ-ray spectra. The $R_{4_1^+ \to 2_1^+}$ takes the value of 0.21(8) for the ^{184}Hg + ^{112}Cd experiment and 0.22(5) for ^{184}Hg + ^{120}Sn. The results are summarized in table 3. The final values were corrected for the K_α/K_β branching ratio and the fluorescence effect.

4.4 Experiment on ^{186}Hg

Similar to the experiments performed for ^{184}Hg, the ^{186}Hg ions were Coulomb excited by three different targets: ^{114}Cd, ^{107}Ag, ^{120}Sn. The γ-ray spectrum following Coulomb excitation of the ^{186}Hg beam on the ^{120}Sn target is presented in fig. 9. A sharp peak around 404 keV was identified as a doublet of the $2_1^+ \to 0_1^+$ and $4_1^+ \to 2_1^+$ γ-ray transitions at the energies of 405 keV and 403 keV, respectively. The 4_2^+ state at the energy of 1080 keV was weakly populated as well: the 675 keV $4_2^+ \to 2_1^+$ and 459 keV $4_2^+ \to 2_2^+$ γ-ray transitions were observed in the

Table 3. Measured γ-ray and K X-ray intensities (not efficiency corrected) for ^{184}Hg scattered on the ^{112}Cd, ^{107}Ag and ^{120}Sn targets. The extracted intensities of the $E0$ $2_2^+ \to 2_1^+$ and $0_2^+ \to 0_1^+$ transitions, corrected for the K_α/K_β X-ray branching ratio and fluorescence effect, are also shown. The angular range for simultaneous detection of two particles is given in the centre-of-mass frame together with the corresponding angular range for the target-nucleus (t) detection in the laboratory frame. The intensities marked with asterisks were derived from the $\gamma\gamma$ analysis (details in the text).

Nucleus	$\Theta_{lab,t}$ ($\Theta_{c.m.}$)	Transition	Counts
^{184}Hg	18.7°–51.6°	$2_1^+ \to 0_1^+$	$2.53(6) \times 10^3$
	(76.8°–142.6°)	$2_2^+ \to 0_1^+$	$1.4(2) \times 10^2$
		$4_1^+ \to 2_1^+$	$1.9(4) \times 10^2$
		K_α (69 keV)	$5.3(5) \times 10^2$
		K_β (80 keV)	76(34)
		$2_2^+ \to 2_1^+$ $E0$	$1.9(15) \times 10^{2*}$
		$0_2^+ \to 0_1^+$	$3.1(17) \times 10^{2*}$
^{112}Cd		$2_1^+ \to 0_1^+$	$4.8(3) \times 10^2$
^{184}Hg	18.2°–50.7°	$2_1^+ \to 0_1^+$	$4.3(20) \times 10^2$
	(78.6°–143.6°)	$2_2^+ \to 0_1^+$	20(7)
		$4_1^+ \to 2_1^+$	40(13)
		K_α (69 keV)	79(16)
^{107}Ag		$3/2_1^- \to 1/2_1^-$	$1.13(19) \times 10^2$
		$5/2_1^- \to 3/2_1^-$	$1.58(14) \times 10^2$
^{184}Hg	18.2°–50.7°	$2_1^+ \to 0_1^+$	$3.60(60) \times 10^3$
	(78.6°–143.6°)	$2_2^+ \to 0_1^+$	$2.50(18) \times 10^2$
		$4_1^+ \to 2_1^+$	$2.8(3) \times 10^2$
		$4_2^+ \to 2_2^+$	20(7)
	doublet:	$2_3^+ \to 0_2^+$	14(7)
		& $2_3^+ \to 2_1^+$	
		K_α (69 keV)	$5.2(4) \times 10^2$
		K_β (80 keV)	$1.8(3) \times 10^2$
		$2_2^+ \to 2_1^+$ $E0$	$4.0(16) \times 10^{2*}$
		$0_2^+ \to 0_1^+$	$1.3(17) \times 10^{2*}$

experiments performed with the ^{107}Ag and ^{120}Sn targets. The low-energy level scheme of ^{186}Hg together with all observed γ-ray transitions in the Coulomb excitation experiment is shown in fig. 10.

The intensity of the $4_1^+ \to 2_1^+$ γ-ray transition was deduced from the $\gamma\gamma$ analysis, analogous to those performed for ^{182,184}Hg. The coincident γ-ray spectrum, gated on the $2_1^+ \to 0_1^+$ and $4_1^+ \to 2_1^+$ doublet in ^{186}Hg, is presented in fig. 11. However, in this case the clear peak vis-

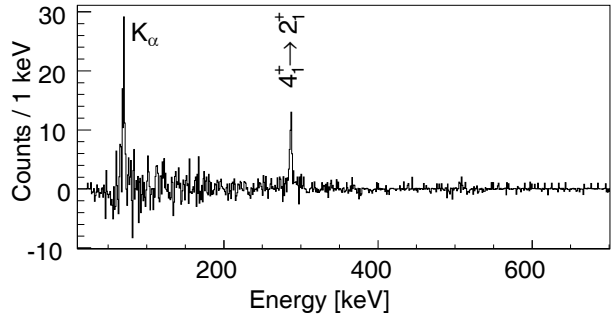

Fig. 8. The random-subtracted, coincident $\gamma\gamma$-ray spectrum obtained for ^{184}Hg excited on the ^{120}Sn target and gated on the $2_1^+ \rightarrow 0_1^+$ transition in ^{184}Hg at the energy of 367 keV. The γ rays were Doppler-corrected for the ^{184}Hg ejectile.

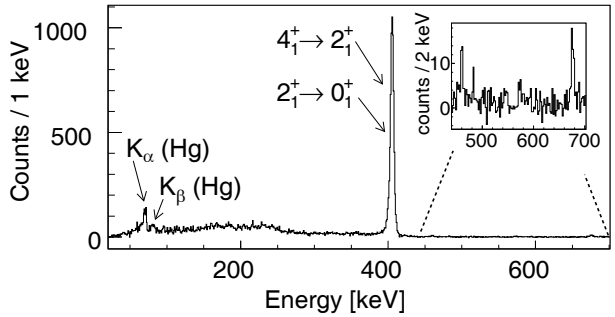

Fig. 9. Two-particle-gated and random-subtracted γ-ray spectrum of ^{186}Hg obtained with the ^{120}Sn target. The γ-ray energies were Doppler-corrected for the ^{186}Hg ejectile. The doublet of $2_1^+ \rightarrow 0_1^+$ and $4_1^+ \rightarrow 2_1^+$ transitions in ^{186}Hg was observed. Inset: the $4_2^+ \rightarrow 2_1^+$ and $4_2^+ \rightarrow 2_2^+$ γ-ray transitions at 675 keV and 459 keV, respectively, are shown.

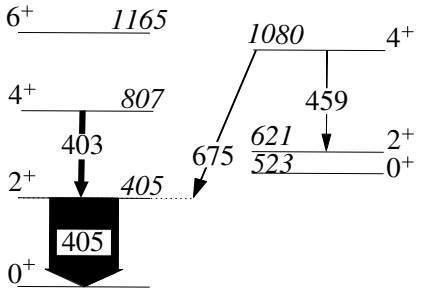

Fig. 10. Low-energy part of the level scheme of ^{186}Hg, relevant to the Coulomb-excitation analysis. Level and γ-ray transition energies are given in keV. Widths of the arrows are proportional to the measured γ-ray yields. Figure adapted from ref. [20].

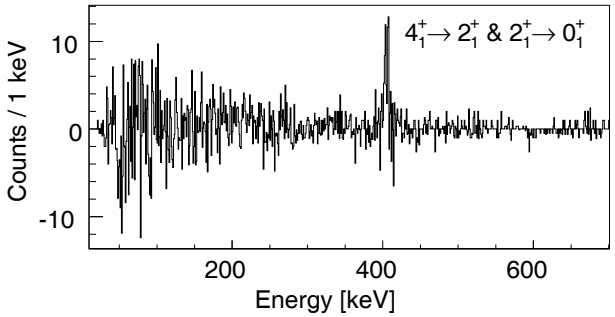

Fig. 11. The random-subtracted $\gamma\gamma$ coincidence spectrum, obtained for ^{186}Hg, Coulomb-excited on the ^{120}Sn target, gated on the $2_1^+ \rightarrow 0_1^+$ and $4_1^+ \rightarrow 2_1^+$ doublet around 404 keV. The γ-ray energies were Doppler-corrected for the ^{186}Hg ejectile.

Table 4. Measured γ-ray and K X-ray intensities (not efficiency-corrected) for ^{186}Hg scattered on the ^{114}Cd, ^{107}Ag and ^{120}Sn targets. The angular range for simultaneous detection of two particles is given in the centre-of-mass frame together with the corresponding angular range for the target-nucleus (t) detection in the laboratory frame. The photo-peak intensities marked with asterisks were derived from the $\gamma\gamma$ coincidence analysis (details are given in the text).

Nucleus	$\Theta_{lab,t}$ ($\Theta_{c.m.}$)	Transition	Counts
^{186}Hg	18.7°–51.6°	$2_1^+ \rightarrow 0_1^+$	$1.56(6) \times 10^3$
	(76.8°–142.6°)	$4_1^+ \rightarrow 2_1^+$	$6(3) \times 10^*$
		K_α (69 keV)	$1.2(3) \times 10^2$
^{114}Cd		$2_1^+ \rightarrow 0_1^+$	$5.7(3) \times 10^2$
^{186}Hg	18.2°–50.7°	$2_1^+ \rightarrow 0_1^+$	$3.22(8) \times 10^3$
	(78.6°–143.6°)	$4_1^+ \rightarrow 2_1^+$	$1.4(5) \times 10^{2*}$
		$4_2^+ \rightarrow 2_1^+$	46(10)
		K_α (69 keV)	$2.5(4) \times 10^2$
^{107}Ag		$3/2_1^- \rightarrow 1/2_1^-$	$1.40(5) \times 10^3$
^{186}Hg	18.2°–50.7°	$2_1^+ \rightarrow 0_1^+$	$6.32(10) \times 10^3$
	(78.6°–143.6°)	$4_1^+ \rightarrow 2_1^+$	$1.6(5) \times 10^{2*}$
		$4_2^+ \rightarrow 2_1^+$	58(13)
		$4_2^+ \rightarrow 2_2^+$	27(14)
		K_α (69 keV)	$4.2(5) \times 10^2$
		K_β (80 keV)	$1.7(4) \times 10^2$

ible at the energy of 404 keV consists of two components: the $2_1^+ \rightarrow 0_1^+$ γ rays in coincidence with the $4_1^+ \rightarrow 2_1^+$ transition and the $4_1^+ \rightarrow 2_1^+$ γ rays in coincidence with the $2_1^+ \rightarrow 0_1^+$ γ-ray transition. Since both cases are just as likely to occur, half of the observed intensity should be attributed to the $4_1^+ \rightarrow 2_1^+$ transition. Details of the analysis are presented in ref. [29]. The extracted intensities are summarized in table 4. The $5/2_1^- \rightarrow 3/2_1^-$ γ-ray transition from the excitation of the ^{107}Ag target nucleus was observed as well. The energy of this transition, 423 keV, is close to those of the $2_1^+ \rightarrow 0_1^+$ and $4_1^+ \rightarrow 2_1^+$ transitions in ^{186}Hg. As a result, a broad structure was observed in the spectrum Doppler-corrected for the ^{107}Ag recoil, which made the precise extraction of the $5/2_1^- \rightarrow 3/2_1^-$ γ-ray intensity not possible [29]. However, the spectrum Doppler-corrected for ^{186}Hg, revealed a clear narrow peak on a broad background for the doublet of the $2_1^+ \rightarrow 0_1^+$ and $4_1^+ \rightarrow 2_1^+$ γ-ray transitions. This allowed determination of the intensity of these two transitions in an unambiguous way.

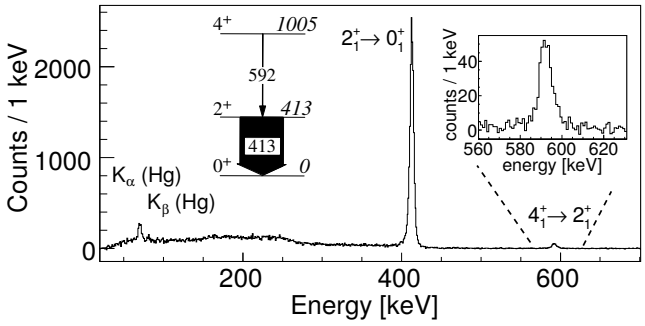

Fig. 12. Two-particle-gated, random-subtracted γ-ray spectra collected for ^{188}Hg, Coulomb-excited by the ^{120}Sn target. The γ-ray energies were Doppler-corrected for the ^{188}Hg ejectile. Left inset: low-energy part of the level scheme of ^{188}Hg, populated in Coulomb-excitation. Level and γ-ray transition energies are given in keV. Widths of the arrows are proportional to the measured γ-ray yields. Figure adapted from ref. [20].

The 2_2^+ state was not populated in the experiment. No 216 keV $2_2^+ \rightarrow 2_1^+$ γ-ray transition was visible in the two-particle-gated γ-ray spectra. The $2_2^+ \rightarrow 2_1^+$ is a relatively highly converted transition with a total conversion coefficient, $\alpha_{tot}(2_2^+ \rightarrow 2_1^+)$, known to be equal 3.5(5) [32]. However, in the contrary to the case of ^{182,184}Hg, the number of K_α X rays in the $\gamma\gamma$ coincidence spectrum is consistent with zero (see fig. 11) indicating that $E0$ de-excitation attributed to the $2_2^+ \rightarrow 2_1^+$ transition was not observed. Nevertheless, all known spectroscopic information concerning the 2_2^+ state was included in the analysis aiming extraction of the matrix elements using the GOSIA code (see sect. 5 for more details).

Some X rays are visible in the two-particle-gated γ-ray spectra, fig. 9. These remain after subtracting X rays originating from the K-vacancy creation and from known internal conversion of the observed γ-ray transitions. They are attributed to the $E0(0_2^+ \rightarrow 0_1^+)$ transition.

4.5 Experiment on ^{188}Hg

In the Coulomb excitation of ^{188}Hg induced by the ^{120}Sn, ^{114}Cd and ^{107}Ag targets, the 2_1^+ and 4_1^+ states in ^{188}Hg were populated (see fig. 12). The beam intensity of 10^5 pps yielded high statistics collected during 11.4 h and 15.9 h of data taking with the ^{120}Sn and ^{114}Cd targets, respectively. Significantly lower statistics were collected during the experiment with the ^{107}Ag target due to a much shorter data collection time compared to the measurements using the ^{120}Sn and ^{114}Cd targets (see table 1). As an example, the total Doppler-corrected and random-subtracted γ-ray spectrum obtained for ^{188}Hg, Coulomb-excited by the ^{120}Sn target, is presented in fig. 12. In the case of the experiment performed with the ^{114}Cd target, the intensity of the 592 keV $4_1^+ \rightarrow 2_1^+$ γ-ray transition in ^{188}Hg could not be extracted since it is contaminated by the Doppler-broadened $2_1^+ \rightarrow 0_1^+$ transition in the ^{114}Cd target at the energy of 558 keV. This was not the case for the experiments performed with the ^{120}Sn and ^{107}Ag targets, where the $4_1^+ \rightarrow 2_1^+$ transition was clearly identified. Moreover, in the $\gamma\gamma$ coincident spectrum there is no indication of a population of higher-lying states, except for the 4_1^+. Particularly, no statistically significant 411 keV $0_2^+ \rightarrow 2_1^+$ γ-ray transition was observed in coincidence with the $2_1^+ \rightarrow 0_1^+$ transition [29]. Weak K X rays are visible in the total γ-ray spectrum in fig. 12. They partially originate from the internal conversion of the observed γ-ray transitions in ^{188}Hg. After subtracting this contribution the remaining number of X rays was attributed to the heavy-ion induced K vacancy creation due to atomic processes and used as a normalization for lighter mercury isotopes (see sect. 4.1 and ref. [27] for more details).

Table 5. Measured γ-ray and K X-ray intensities (not efficiency-corrected) for ^{188}Hg scattered on the ^{114}Cd, ^{107}Ag and ^{120}Sn targets. The angular range for simultaneous detection of two particles is given in centre-of-mass frame together with the corresponding angular range for the target-nucleus (t) detection in laboratory frame.

Nucleus	$\Theta_{lab,t}$ ($\Theta_{c.m.}$)	Transition	Counts
^{188}Hg	18.7°–51.6° (76.8°–142.6°)	$2_1^+ \rightarrow 0_1^+$	$1.239(13) \times 10^4$
		K_α (69 keV)	$8.0(8) \times 10^2$
^{114}Cd		$2_1^+ \rightarrow 0_1^+$	$4.70(8) \times 10^3$
^{188}Hg	18.2°–50.7° (78.6°–143.6°)	$2_1^+ \rightarrow 0_1^+$	$2.02(5) \times 10^3$
		$4_1^+ \rightarrow 2_1^+$	48(11)
		K_α (69 keV)	98(25)
^{107}Ag		$3/2_1^- \rightarrow 1/2_1^-$	$9.8(4) \times 10^2$
^{188}Hg	18.2°–50.7° (78.6°–143.6°)	$2_1^+ \rightarrow 0_1^+$	$1.579(14) \times 10^4$
		$4_1^+ \rightarrow 2_1^+$	$4.5(3) \times 10^2$
		K_α (69 keV)	$9.2(9) \times 10^2$
		K_β (80 keV)	$1.4(6) \times 10^2$

The γ-ray and K X-ray intensities in ^{188}Hg extracted from the Coulomb-excitation experiments are given in table 5. Similar to ^{186}Hg + ^{107}Ag experiment, the unambiguous extraction of the 423 keV, $5/2_1^- \rightarrow 3/2_1^-$ γ-ray transition in ^{107}Ag was not possible. The energy of this transition is close to the 413 keV, $2_1^+ \rightarrow 0_1^+$ transition in ^{188}Hg, which forms a broad structure in the spectrum Doppler-corrected for the ^{107}Ag recoil. However, as in the previous case, the spectrum Doppler-corrected for ^{188}Hg revealed a clear narrow peak for the $2_1^+ \rightarrow 0_1^+$ γ-ray transition on a broad background, allowing precise extraction of its intensity.

5 Matrix elements determination

In order to determine the $E2$ matrix elements in ^{182,184,186,188}Hg, the Coulomb-excitation least-squares fitting code GOSIA [33, 34] was used. The code constructs a standard χ^2 function built of measured γ-ray intensities and those calculated from a set of matrix elements

between all relevant states. Additionally, known spectroscopic data, *e.g.*, γ-ray branching ratios, multipole mixing coefficients and lifetimes, can be used as auxiliary data in the minimization procedure. These data enter the χ^2 function on an equal basis as γ-ray intensities observed in the Coulomb-excitation experiments.

The γ-ray branching ratios known from the β-decay studies of ^{182,184,186,188}Tl isotopes [17, 35–37] were used in the GOSIA analysis as additional data points serving as important constraints in the multidimensional χ^2 fit. Moreover, the $E0$ transitions were included as well, together with the known total conversion coefficients for the $2_2^+ \rightarrow 2_1^+$ transitions in ^{182,184}Hg [17] and ^{186}Hg [32], as described in more detail in sect. 5.2. Lifetimes of the yrast states in ^{182,184,186}Hg were measured independently using the RDDS method [19, 38, 39]. Lifetimes of excited states in ^{182}Hg were extracted in ref. [38] and in ref. [39]. Both publications report consistent results which were obtained by applying two different analysis procedures to the same data set. In the current Coulomb-excitation analysis we used lifetime values from ref. [39]. Lifetimes of the non-yrast 0_2^+ and 2_2^+ states in ^{186,188}Hg were taken from ref. [40].

Since lifetimes provide strong constraints in the multidimensional GOSIA fit, it was important to check the consistency between them and the Coulomb-excitation data. Thus, at the first stage of analysis no lifetime information was included and the Coulomb-excitation cross sections for the projectile were normalized to the known excitation cross sections for target nuclei. These calculations were performed with the GOSIA2 code [34], which is a modified version of the standard GOSIA code, capable of handling mutual excitation of target and projectile nuclei. The method is described in detail in ref. [41] and recently has been applied as well in refs. [42–44]. The analysis of the Coulomb-excitation data performed without using the known lifetimes of excited states in ^{182,184,186}Hg yielded results consistent within 1σ uncertainty with the lifetime values [29].

To exploit the dependence of the Coulomb-excitation probability on the scattering angle, and in this way gain the sensitivity to higher-order-effects, such as quadrupole moments or signs of the interference terms, the data for each mercury isotope were subdivided, depending on the experiment, into three or five subsets. They corresponded to different angular ranges of scattered particle. The influence of the scattering angle on multi-step excitation probability is illustrated in fig. 13, where an increase of the $4_1^+ \rightarrow 2_1^+$ γ-ray yield with respect to the $2_1^+ \rightarrow 0_1^+$ transition is observed for higher center-of-mass angles. The division of the data was a compromise between the number of independent data points for the γ-ray yields and the level of statistics obtained for the individual ranges. Due to the low statistics collected in the experiments with the ^{107}Ag target, no divisions were applied to these data. Instead, the total intensities were used in the analysis. The same applies to the $2_2^+ \rightarrow 2_1^+$ γ-ray and the $E0$ in ^{182,184}Hg.

The current work presents the re-evaluated values, with respect to refs. [20, 29], of matrix elements in ^{182,184}Hg, obtained using revised spectroscopic data characterizing the low-energy structure of these isotopes that have recently become available [17] and which differ from the values used in the previous analysis [20]. The change concerns mainly the values of the total conversion coefficients $\alpha_{tot}(2_2^+ \rightarrow 2_1^+)$ which is equal to 7.2(13) in ^{182}Hg and 14.2(36) in ^{184}Hg, (instead of the values of 4.7(13) and 23(5) for ^{182}Hg and ^{184}Hg, respectively, that were used in the previous analysis), as well as the $2_2^+ \rightarrow 0_2^+/2_2^+ \rightarrow 0_1^+$ γ-ray branching ratio in ^{184}Hg which changes from 0.082(34) to 0.016(9). The new analysis together with the obtained matrix elements is presented in detail in sect. 5.1.

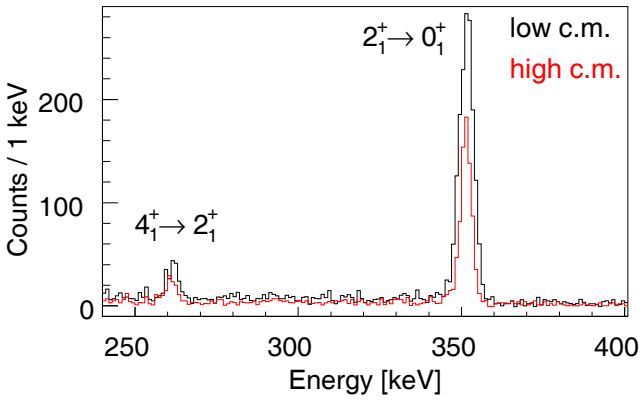

Fig. 13. (Color online) The γ-ray spectra after Coulomb excitation of ^{182}Hg on ^{112}Cd for two subsets of data corresponding to low (76.8°–92.8°, black) and high (114.4°–142.6°, red) center-of-mass scattering angles, respectively. The spectra are Doppler-corrected for the ^{182}Hg ejectile and random-subtracted.

Table 6. Experimentally determined signs of interference terms in ^{182}Hg and ^{184}Hg. For the sign of the $\langle 2_1^+ \| E2 \| 2_2^+ \rangle \langle 2_2^+ \| E2 \| 0_2^+ \rangle \langle 0_2^+ \| E2 \| 2_1^+ \rangle$ product in ^{182}Hg no conclusive results can be given.

Interference term	^{182}Hg	^{184}Hg
$\langle 0_1^+ \| E2 \| 2_1^+ \rangle \langle 2_1^+ \| E2 \| 2_2^+ \rangle \langle 2_2^+ \| E2 \| 0_1^+ \rangle$	+	+
$\langle 0_2^+ \| E2 \| 2_1^+ \rangle \langle 2_1^+ \| E2 \| 2_2^+ \rangle \langle 2_2^+ \| E2 \| 0_2^+ \rangle$		−
$\langle 2_1^+ \| E2 \| 4_1^+ \rangle \langle 4_1^+ \| E2 \| 2_2^+ \rangle \langle 2_2^+ \| E2 \| 2_1^+ \rangle$	−	−

5.1 Analysis of ^{182}Hg and ^{184}Hg

The level schemes of ^{182}Hg and ^{184}Hg, limited to well-known states considered in the current analysis, are presented in figs. 4 and 7, respectively. The measured γ-ray yields, listed in tables 2 and 3, as well as the $E0$ transitions extracted between the pairs of 0^+ and pairs of 2^+ states in ^{182,184}Hg, were included in the GOSIA analysis. The method adopted to include the $E0$ decay in the GOSIA analysis is described in detail in sect. 5.2. In total, 19[14] transitional and diagonal matrix elements were fitted to 40[20] data points in ^{184}Hg [^{182}Hg].

The analysis of the Coulomb-excitation data brings information on the relative signs of transition matrix elements, as the latter may have a significant influence

Table 7. Reduced matrix elements obtained in this work for ^{182}Hg and ^{184}Hg. The $E2$ matrix elements for ^{186,188}Hg are taken from ref. [20]. The relative signs of matrix elements were determined by analysing the influence of interference terms listed in table 6. The adopted sign convention enables a direct comparison with the two-state mixing model calculations presented in sect. 6.3.

$\langle I_i \Vert E2 \Vert I_f \rangle$ (eb)	^{182}Hg	^{184}Hg	^{186}Hg	^{188}Hg
$\langle 0_1^+ \Vert E2 \Vert 2_1^+ \rangle$	1.29(4)	1.27(3)	$1.25^{+0.10}_{-0.07}$	1.31(10)
$\langle 2_1^+ \Vert E2 \Vert 4_1^+ \rangle$	3.70(6)	3.31(6)	3.4(2)	2.07(8)
$\langle 0_1^+ \Vert E2 \Vert 2_2^+ \rangle$	−0.6(1)	0.348(14)	(±) 0.05(1)	
$\langle 0_2^+ \Vert E2 \Vert 2_1^+ \rangle$	$[-2.2, 0.9]$	$-1.2^{+0.3}_{-0.2}$		
$\langle 0_2^+ \Vert E2 \Vert 2_2^+ \rangle$	−1.25(30)	$0.93^{+0.20}_{-0.25}$	≥ 2.9	
$\langle 2_1^+ \Vert E2 \Vert 2_2^+ \rangle$	−2.0(3)	$1.64^{+0.14}_{-0.16}$		
$\langle 2_2^+ \Vert E2 \Vert 4_1^+ \rangle$	3.3(4)	$[-3, 0]^\star$	$-5.3^{+1.3}_{-0.5}$	
$\langle 2_1^+ \Vert E2 \Vert 2_1^+ \rangle$				$1.0^{+0.6}_{-0.4}$
$\langle 2_2^+ \Vert E2 \Vert 2_2^+ \rangle$				

* The value of $\langle 2_2^+ \Vert E2 \Vert 4_1^+ \rangle$ in ^{184}Hg is $-3 \leq \langle 2_2^+ \Vert E2 \Vert 4_1^+ \rangle < 0$.

on the Coulomb-excitation cross sections. The absolute sign of an individual transitional matrix element has no physical meaning, since it depends on the arbitrary choice of the relative phases of wave functions of initial and final states. However, the sign of the product of the matrix elements–the so called interference term *e.g.*, $\langle 0_1^+ \Vert E2 \Vert 2_2^+ \rangle \langle 2_2^+ \Vert E2 \Vert 2_1^+ \rangle \langle 2_1^+ \Vert E2 \Vert 0_1^+ \rangle$ —is independent of the chosen convention and can be determined experimentally. The signs of three interference terms were determined for ^{182}Hg and ^{184}Hg and are listed in table 6. A convention adopted in the case of ^{182}Hg was that the signs of all transitional $E2$ matrix elements connecting the yrast states and the $E2$ matrix elements between the non-yrast states, as well as the sign of the $\langle 2_2^+ \Vert E2 \Vert 2_1^+ \rangle$ matrix element, were fixed. The signs of all the remaining matrix elements were free, *i.e.*, the signs of the interference terms could be determined in the GOSIA analysis. A similar approach was used for ^{184}Hg.

The relative signs of the matrix elements reported in the present work for ^{182,184}Hg were verified by performing the minimization procedure for all possible sign combinations of the interference terms. The obtained χ^2 values were compared. For example, when the $\langle 0_1^+ \Vert E2 \Vert 2_1^+ \rangle \langle 2_1^+ \Vert E2 \Vert 2_2^+ \rangle \langle 2_2^+ \Vert E2 \Vert 0_1^+ \rangle$ product in ^{182}Hg is negative, it causes a four-fold increase in the total χ^2 value as compared to the positive sign of this term. Only in the case of the $\langle 2_1^+ \Vert E2 \Vert 2_2^+ \rangle \langle 2_2^+ \Vert E2 \Vert 0_2^+ \rangle \langle 0_2^+ \Vert E2 \Vert 2_1^+ \rangle$ interference term in ^{182}Hg two equally deep χ^2 minima corresponding to the different signs of this product were found. The main difference between the sets of matrix elements for these two minima are the opposite signs of the $\langle 0_2^+ \Vert E2 \Vert 2_1^+ \rangle$ matrix element. The signs of all other transitional $E2$ matrix elements are the same, and only slight differences in their magnitudes are observed. The uncertainties of the matrix elements reported in table 7 account for these small variations. The value of the $\langle 0_2^+ \Vert E2 \Vert 2_1^+ \rangle$ matrix element in ^{182}Hg is given as a range.

The resulting set of reduced matrix elements in ^{182,184}Hg together with their relative signs is presented in table 7. The estimation of the statistical uncertainties of the matrix elements was performed in two steps. Firstly, the uncorrelated uncertainties were calculated. Then, all possible correlations between the matrix elements were taken into account. The final confidence interval, defined by the integral of probability distribution, is equal to 68.3% [33].

The differences between the re-evaluated values of the matrix elements and those published in ref. [20] mainly stem from the change in $\alpha_{tot}(2_2^+ \rightarrow 2_1^+)$ and γ-ray branching ratios, as explained above. The values of the matrix elements related to the 2_2^+ and 0_2^+ states are most influenced by these changes. The reduced matrix elements obtained for ^{182,184}Hg reproduce all γ-ray branching ratios, total conversion coefficients $\alpha_{tot}(2_2^+ \rightarrow 2_1^+)$ and lifetimes within the 1σ uncertainty. Almost all experimental γ-ray yields were reproduced within 1σ uncertainty. The only exceptions are: (i) $I(2_2^+ \rightarrow 0_1^+)$ in ^{184}Hg for the experiment with the ^{107}Ag target reproduced within 1.3σ, (ii) $I(4_1^+ \rightarrow 2_1^+)$ in ^{184}Hg reproduced within 1.5σ in one of the experimental data sets with the ^{112}Cd target, (iii) $I(E0, 2_2^+ \rightarrow 2_1^+)$ in ^{182}Hg reproduced within 2σ.

The diagonal matrix elements of the 2_1^+, 2_2^+ and 4_1^+ states were included in the analysis as free parameters. With the new, revised spectroscopic data, a careful analysis of the signs of the $2_{1,2}^+$ diagonal matrix elements was performed for ^{182}Hg and ^{184}Hg. This analysis shows that changes in the value and/or sign of a given diagonal matrix element, for example from 1.1 eb to −1.6 eb for $\langle 2_1^+ \Vert E2 \Vert 2_1^+ \rangle$ in ^{184}Hg, do not significantly influence neither other values of the transitional $E2$ matrix elements, nor the quality of the χ^2 fit. Furthermore, because of the large uncertainty related to the $E0$ component of the $2_2^+ \rightarrow 2_1^+$ transition in ^{182,184}Hg we refrain from reporting

any diagonal matrix elements for the 2^+ states except for the ^{188}Hg. In the latter case, extraction of the $\langle 2_1^+ \| E2 \| 2_1^+ \rangle$ matrix element is more straightforward, since only 2_1^+ and 4_1^+ states were populated in ^{188}Hg. For the comparison with the quadrupole sum rules results presented in fig. 3 of ref. [20], the $\langle Q^3 \cos(3\delta) \rangle$ invariant cannot be determined from the current results; consequently, no conclusion on the triaxiality of the 0^+ states can be drawn. However, the values of the $\langle Q^2 \rangle$ invariants, analogous to those reported in ref. [20], can be extracted for the 0^+ states from the $E2$ matrix elements presented in table 7. The $\langle Q^2 \rangle$ values for the 0_1^+ states in ^{182}Hg and ^{184}Hg are equal to 2.04(16) e^2b^2 and 1.74(15) e^2b^2, respectively and are consistent with those published in ref. [20]. For the excited 0^+ states the $\langle Q^2 \rangle = 2.3(9)$ e^2b^2 in ^{184}Hg and an upper limit of 7.1 e^2b^2 can be given for ^{182}Hg. The latter are in a better agreement with equivalent values calculated with the beyond-mean-field and the interacting boson models as shown in fig. 3 in ref. [20]. It is worth to mention that while the $\langle Q^2 \rangle$ invariant for the ground state in even-even nuclei is almost completely determined by the $\langle 0_1^+ \| E2 \| 2_1^+ \rangle$ matrix element [45], the situation becomes more complex for the higher-order invariant, *i.e.* $\langle Q^3 \cos(3\delta) \rangle$, as discussed in refs. [43, 45]. In order to extract the latter for the $0_{1,2}^+$ states, knowledge on diagonal matrix elements of the excited 2^+ states is particularly important as well as information about signs of all relevant interference terms.

The $E2/M1$ mixing ratios, $\delta(\frac{E2}{M1})$, are not known for any transitions between the low-lying states in ^{182,184}Hg. In the current analysis the $2_3^+ \rightarrow 2_1^+$ and $4_2^+ \rightarrow 4_1^+$ transitions in ^{184}Hg were assumed to be of pure $E2$ character. In the case of the $2_2^+ \rightarrow 2_1^+$ transition in ^{182,184}Hg, a $\delta(\frac{E2}{M1})$ value of 1.85 was adopted, consistent with the known value in ^{202}Po [46]. An influence of the unknown $E2/M1$ mixing ratio on the extracted $E2$ matrix elements was investigated. The $E2/M1$ ratio was varied over several values between 0.5 and 5. For each value of the mixing ratio, $\delta(\frac{E2}{M1})$, a full minimization with the GOSIA code was performed. The solutions obtained with $\delta(\frac{E2}{M1}) > 1$ correspond to similar χ^2 values and no considerable change in other $E2$ matrix elements in ^{182,184}Hg was observed. A larger change in values of the matrix elements related to the 2_2^+ state is observed when $\delta(\frac{E2}{M1}) < 1$, as presented in fig. 14.

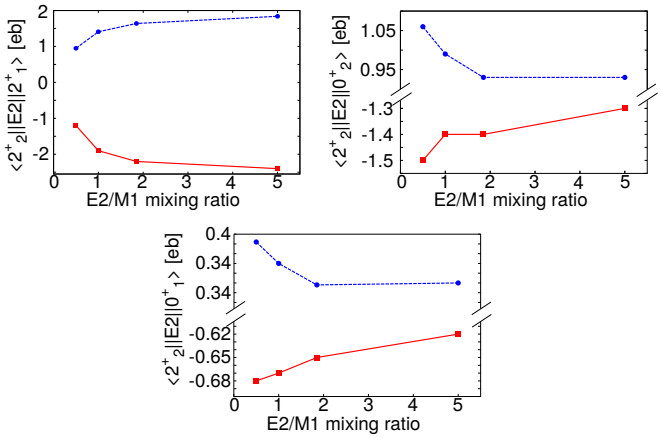

Fig. 14. (Color online) $E2$ and $M1$ matrix elements related to the 2_2^+ state in ^{182}Hg (red solid line) and ^{184}Hg (blue dashed line) resulting from the Coulomb-excitation data analysis performed assuming different values of the $E2/M1$ mixing ratio for the $2_2^+ \rightarrow 2_1^+ \gamma$-ray transition.

5.2 Implementation of the E0 decay into the GOSIA analysis

The analysis of the intense K X-ray peaks measured for ^{182,184}Hg revealed that the $2_2^+ \rightarrow 2_1^+$ transitions are strongly converted. Furthermore, the intensities of the $0_2^+ \rightarrow 0_1^+$ and $2_2^+ \rightarrow 2_1^+$ $E0$ transitions in ^{182,184}Hg were deduced. Moreover, the total conversion coefficient of the $2_2^+ \rightarrow 2_1^+$ transition, $\alpha_{tot}(2_2^+ \rightarrow 2_1^+)$, measured in β/EC decay of ^{182,184}Tl [17] was extracted for ^{182}Hg and ^{184}Hg. Such data are crucial for the Coulomb-excitation analysis, as transitions under investigation contain large $E0$ components, which need to be taken into account when extracting matrix elements. As it is not currently possible to declare the $E0$ transitions directly in the GOSIA input files, an indirect method was applied, which has also been tested before *e.g.*, in refs. [43,44]. The $E0$ decay path of the 0_2^+ state was simulated in the fit by an $M1$ transition via a virtual 1^+ state, introduced in addition to the known level schemes of ^{182,184}Hg. The extra 1_1^+ states were placed below the 0_2^+ state, at 259 keV and 306 keV excitation energy in ^{182}Hg and ^{184}Hg, respectively, and connected to the 0_2^+ state by a 69 keV $M1$ transition. The choice of the excitation energy for the virtual 1^+ state is arbitrary. However, it was checked that changing this excitation energy does not influence the final results. The virtual $0_2^+ \rightarrow 1_1^+$ $M1$ transition is utilised to enable the $E0$ decay path of the 0_2^+ state. The $\langle 0_2^+ \| M1 \| 1_1^+ \rangle$ matrix element was introduced in the GOSIA input file, together with the $\langle 1_1^+ \| M1 \| 0_1^+ \rangle$ matrix element enabling depopulation of the 1_1^+ state.

In a similar way the $E0$ component of the $2_2^+ \rightarrow 2_1^+$ transition was taken into account. A second additional 1_2^+ state was included in the level schemes of ^{182}Hg and ^{184}Hg, placed between the first two 2^+ states at the energy of 479 keV and 465 keV, respectively. The $M1$ matrix elements connecting the $2_{1,2}^+$ states with the 1_2^+ states were introduced as well. Since low-energy Coulomb excitation proceeds predominantly via $E2$ (and $E3$) transitions, the introduction of these additional matrix elements does not influence the calculated excitation pattern. In contrast, the $M1$ transitions strongly influence the de-excitation process.

The branching ratio, which represents in the analysis the $\alpha_{tot}(2_2^+ \rightarrow 2_1^+)$, is interpreted as the ratio of the $I(E0; 2_2^+ \rightarrow 2_1^+)$ intensity and the $2_2^+ \rightarrow 2_1^+$ γ-ray intensity of mixed $E2/M1$ multipolarity,

$$BR\left(\frac{2_2^+ \rightarrow 1_2^+}{2_2^+ \rightarrow 2_1^+}\right) = \frac{I^{E0}(2_2^+ \rightarrow 2_1^+)}{I_\gamma^{E2+M1}(2_2^+ \rightarrow 2_1^+)}\,. \qquad (2)$$

This can be further expressed by the total conversion coefficient $\alpha_{tot}(2_2^+ \to 2_1^+)$,

$$BR\left(\frac{2_2^+ \to 1_2^+}{2_2^+ \to 2_1^+}\right) = \alpha_{tot}(2_2^+ \to 2_1^+) - \frac{I_\gamma^{E2}(2_2^+ \to 2_1^+) \cdot \alpha(E2; 2_2^+ \to 2_1^+)}{I_\gamma^{E2+M1}(2_2^+ \to 2_1^+)} - \frac{I_\gamma^{M1}(2_2^+ \to 2_1^+) \cdot \alpha(M1; 2_2^+ \to 2_1^+)}{I_\gamma^{E2+M1}(2_2^+ \to 2_1^+)}. \quad (3)$$

As the experimental $E0$ intensity $I^{E0}(2_2^+ \to 2_1^+)$ is known for ^{182}Hg and ^{184}Hg, it needs to be taken into account as well. Such data were included in the analysis assuming that the $E0$ de-excitation of the 2_2^+ proceeds via the $2_2^+ \to 1_2^+$ transition

$$I^{E0}(2_2^+ \to 2_1^+) = I_\gamma^{M1}(2_2^+ \to 1_2^+) + I_e^{M1}(2_2^+ \to 1_2^+). \quad (4)$$

As the $E0$ components are represented in the GOSIA analysis by $M1$ γ-ray transitions, the experimental intensity $I^{E0}(2_2^+ \to 2_1^+)$ needs to be corrected for internal conversion as follows:

$$I^{E0,corr}(2_2^+ \to 2_1^+) = \frac{I^{E0}(2_2^+ \to 2_1^+)}{1 + \alpha(M1; 2_2^+ \to 1_2^+)}. \quad (5)$$

Similarly for the $I^{E0}(0_2^+ \to 0_1^+)$ intensity:

$$I^{E0,corr}(0_2^+ \to 0_1^+) = \frac{I^{E0}(0_2^+ \to 0_1^+)}{1 + \alpha(M1; 0_2^+ \to 1_1^+)}. \quad (6)$$

Correcting for the experimental intensity $I^{E0}(2_2^+ \to 2_1^+)$ given by eq. (5) and expressing the $\frac{I_\gamma^{E2}}{I_\gamma^{E2}+I_\gamma^{M1}}$ term in eq. (3) by the $E2/M1$ mixing ratio δ, one obtains

$$BR\left(\frac{2_2^+ \to 1_2^+}{2_2^+ \to 2_1^+}\right) = \left[\alpha_{tot}(2_2^+ \to 2_1^+) - \frac{\delta^2}{\delta^2+1} \cdot \alpha(E2; 2_2^+ \to 2_1^+) - \frac{1}{\delta^2+1} \cdot \alpha(M1; 2_2^+ \to 2_1^+)\right] \cdot \frac{1}{1 + \alpha(M1; 2_2^+ \to 1_2^+)}. \quad (7)$$

The value of the branching ratio given by eq. (7) was introduced in the GOSIA input file as an additional data point; in this way the total conversion coefficient $\alpha_{tot}(2_2^+ \to 2_1^+)$ was included in the fit. As described in sect. 5, the value of $\delta(\frac{E2}{M1}) = 1.85$ was adopted.

The $\langle 2_2^+ \| M1 \| 1_2^+ \rangle$ matrix elements in ^{182,184}Hg were fitted in such a way that the best reproduction of the experimental $E0$ $2_2^+ \to 2_1^+$ intensities and $BR(\frac{2_2^+ \to 1_2^+}{2_2^+ \to 2_1^+})$ values defined by eq. (7) was achieved. Similar, the $\langle 0_2^+ \| M1 \| 1_1^+ \rangle$ matrix elements were fitted to reproduce the experimentally determined $E0$ $0_2^+ \to 0_1^+$ intensities.

The use of the $M1$ multipolarity to represent the $E0$ decay paths is an arbitrary choice. Other possibilities for the virtual transitions simulating $E0$ decay, *e.g.*, $M2$ transitions, were also tested and no influence on the final solution was observed [29].

6 Results and comparison with three models

6.1 Theoretical tools

In the following section the experimental and theoretical results concerning excitation energies, reduced transition probabilities and spectroscopic quadrupole moments are compared and discussed within the framework of three different models: i) a quadrupole collective model based on the General Bohr Hamiltonian (GBH) [21], ii) a beyond-mean-field model (BMF) [16], and iii) an interacting-boson model with configuration mixing (IBM-CM) [22]. An effective Skyrme interaction is employed in both the GHB and BMF approaches used here, and both methods are based on a set of BCS-type self-consistent mean-field states that cover a wide range of quadrupole deformations.

A BMF calculation consists of several consecutive steps. First, a set of deformed mean-field states with different axial quadrupole moments is constructed by solving the Hartree-Fock plus Bardeen-Cooper-Schrieffe (HF+BCS) equations with suitably chosen constraints. Each of these states is then projected on the proton and neutron numbers of interest and the targeted angular momenta. In the final step, the resulting symmetry-restored states of the same I are mixed in the framework of the generator-coordinate method (GCM). The projection not only provides a spectrum of states with different angular momenta, but it also restores the selection rules for transitions between them. The GCM describes the shape fluctuations of the collective states and also yields a set of orthogonal states, so that their properties can be directly compared with experiment. Since there is no truncation of the model space in BMF models like the 2 $\hbar\omega$ truncation in the shell model space, there is no need to introduce effective charges and the matrix elements of the $E0$ and $E2$ operators are calculated with bare charges. At each step of the calculation, the SLy6 parametrization of the Skyrme interaction is used in connection with a surface-type pairing interaction. For a more detailed description of the calculations, we refer to ref. [16].

A general theory of the collective quadrupole model employing the general Bohr Hamiltonian can be found in ref. [21], while a detailed report on an application of the model is presented in ref. [45]. Here we briefly recall some of its main points. The β and γ dynamical variables of the model, which describe the deformation of a nucleus in the so-called intrinsic frame, are directly related to a quadrupole tensor of the nuclear-mass distribution (however, with no specific shape assumed). All quadrupole degrees of freedom, including nonaxiality and rotations, are

treated on an equal footing. The General Bohr Hamiltonian is determined by seven functions: the potential energy and six inertial functions. These seven functions are calculated from the microscopic mean-field theory using the Adiabatic Time-Dependent Hartree-Fock-Bogoliubov (ATDHFB) approach. The $E2$ electromagnetic transitions are described by a collective operator directly related to the nuclear charge distribution. The computational details are the same as in ref. [45]. Mean-field configurations for given deformations are obtained through constrained HFB calculations using the SLy4 variant of the Skyrme force and the seniority (constant G) force as a pairing interaction. Neither the BMF nor the GBH model contain any free parameter, the value of which would be fixed by comparison with the properties of the excited states considered here.

The GBH can be regarded as a computation friendly approximation of a symmetry-restored GCM. Its space of dynamical variables includes the full $\beta-\gamma$ plane and thus triaxial shapes. The use of ATDHFB masses in the GBH incorporates some effects that in a projected GCM would require consideration of time-reversal-breaking cranked states, which up to now has never been done in a systematic way. The SLy4 interaction used in the GBH is in many respects very similar to the SLy6 interaction used in the BMF calculations; they are fitted with the same protocol, but with a different recipe to correct for the center-of-mass motion. In consequence, SLy6 has a smaller surface-energy coefficient than SLy4, leading to deformation-energy surfaces that are slightly softer [47]. This tends to reduce the excitation energy of coexisting shapes of different deformations, which is one of the possible reasons of some of the differences between the results obtained with the BMF and GBH approaches reported below.

The interacting-boson model [48] is a leading algebraic model approach, making use of the U(6) symmetry of an interacting system built from $L = 0$ and $L = 2$ (s and d) bosons. The IBM is a symmetry-dictated truncation of the nuclear shell model where the bosons represent pairs of fermions. The number of bosons can be related to the number of valence protons and neutrons present in the corresponding shell-model space $N = \frac{n_\pi+n_\nu}{2}$. An extended version of the IBM model, which can be applied when approaching closed shells, is presented in refs. [49, 50]. In this version of the model one includes additional bosons, which are related with possible m-particle n-hole excitations. Consequently, the full model space also contains a part built from $N + 2$ bosons (for $m = 2$ and $n = 2$). The interaction amongst the N and $N + 2$ parts within the full model space gives rise to what is called the IBM-CM model.

Extensive use has been made of the interacting boson model with configuration mixing ([1] and references therein) in various regions of the nuclear chart, with particular attention to the isotopic chains in the Pb region. This approach gives the possibility to describe modes of excitations that exhibit different collective characters. The application to the neutron-deficient Hg nuclei was discussed in detail in ref. [22], where both the construction of the Hamiltonian, the $E2$ operator as well as an extensive discussion of the results have been presented at length.

6.2 Energy spectra and electric quadrupole properties

Experimental and theoretical results concerning the electromagnetic structure of ^{182,184,186,188}Hg nuclei are compared in fig. 15. Energies, $B(E2)$ reduced transition probabilities and spectroscopic quadrupole moments are given for the yrast and the first excited states with even spin I. The quadrupole properties are summarized in table 8. The experimental values for the yrast transition probabilities above the 4_1^+ state in ^{182,184,186}Hg are taken from refs. [19] and [38]. Those for the transitions between the yrast and the first excited 0^+ and 2^+ states in ^{188}Hg are taken from ref. [51].

In the BMF calculations, the wave function for each state is obtained by mixing the deformed mean-field wave functions projected on the same angular momentum and particle numbers. Looking at fig. 9 of ref. [16], one can see that the BMF $I = 0$ states have particularly complicated structures. The only case where the ground state is dominated by the projected prolate configurations is ^{182}Hg. Even in this case, the first excited 0^+ state involves projected oblate and prolate configurations with similar weights. At higher spin, the shape mixing decreases and starting at $I = 6$ (sometimes $I = 4$) either projected oblate or prolate configurations dominate the BMF wave functions. This is reflected in fig. 15 by the fact that the spectroscopic quadrupole moments do not vary much with increasing spin for the highest spin states. The same can be noticed for GBH results.

Both BMF and GBH energy spectra are too spread out compared to the experimental data. A well-known deficiency of these models is that they systematically underestimate moments of inertia. This is generally attributed to the conservation of time-reversal invariance imposed on the mean-field states. This prevents the reduction of pairing and the alignment of single-particle states to be taken into account when performing the projection on finite angular momenta.

The spectroscopic quadrupole moments of the yrast 2^+ states are negative for the BMF and GBH approaches pointing to predominantly prolate states. The only exception is the BMF result for ^{188}Hg, where the spectroscopic quadrupole moment is positive and the calculation slightly overestimates the experimental value. The wave function of this 2^+ state is predominantly composed of projected oblate mean-field states, as are those of the heavier Hg isotopes (see fig. 9 and fig. 17 of ref. [16]). The $B(E2)$ values are systematically overestimated, both in BMF and GBH calculations. This deficiency can have several causes. The most probable ones are either too large weights of projected deformed prolate wave functions or an overestimation of the deformation already at the mean-field level. As discussed in ref. [16] these problems are ultimately linked to the wrong relative position of the single-particle levels at sphericity. Unfortunately, these positions cannot be improved by an obvious change in the parametrizations of the EDFs.

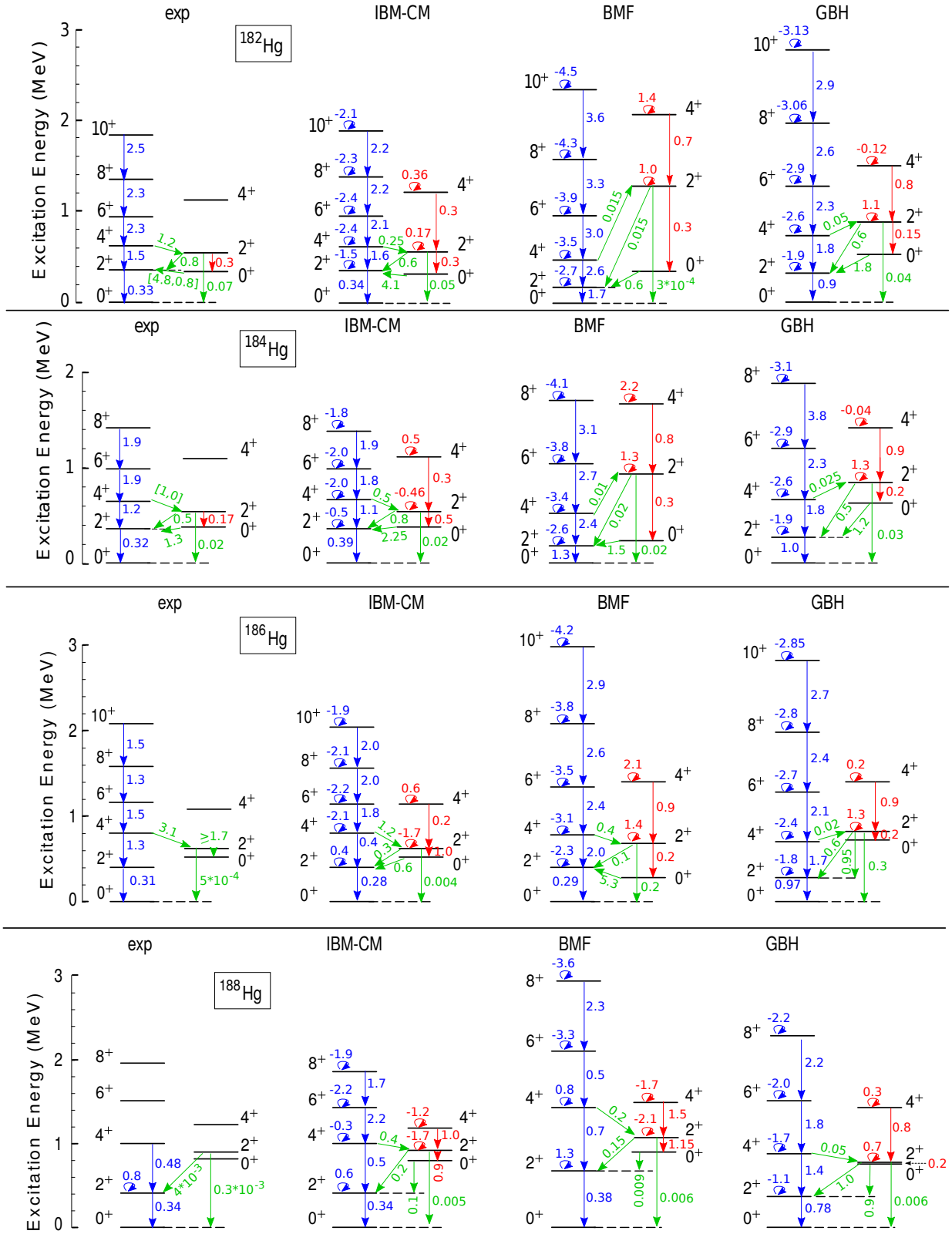

Fig. 15. (Color online) Comparison of the experimental low-energy structures of $^{182-188}$Hg with theoretical IBM-CM [22], BMF [16] and GBH [21,52] predictions. Reduced $E2$ transition probabilities (arrows) and spectroscopic quadrupole moments (loops) are given in e^2b^2 and eb units, respectively. The experimental values are taken from table 8 and refs. [19,38,51]. In each spectrum the left part presents the yrast levels, while the non-yrast states are displayed on the right side. Blue (red) is used for transitions and moments connecting the yrast (non-yrast) states. Transitions between yrast and non-yrast states are marked in green.

Table 8. Reduced $B(E2)$ transition probabilities in ^{182,184,186,188}Hg and spectroscopic quadrupole moments (Q_S) in ^{188}Hg given in $e^2\mathrm{b}^2$ and $e\mathrm{b}$ units, respectively, compared to the results of calculations performed with IBM-CM [22], BMF [16] and GBH [21, 52] models. Experimental values are obtained from Coulomb-excitation and lifetime measurements [19] (^{b}), [38] (^{a}). Values for transitions marked with index (^{c}) are taken from ref. [51].

			$B(E2; I_i \to I_f)$ $[e^2\mathrm{b}^2]$			
Isotope	I_i	I_f	Experiment	IBM	BMF	GBH
^{182}Hg	2_1^+	0_1^+	0.33(2)	0.34	1.68	0.88
	4_1^+	2_1^+	1.52(5)	1.6	2.61	1.8
	6_1^+	4_1^+	$2.27(18)^a$	2.07	2.98	2.29
	8_1^+	6_1^+	$2.33(25)^a$	2.17	3.27	2.64
	10_1^+	8_1^+	$2.45(61)^a$	2.18	3.55	2.94
	2_2^+	0_1^+	0.072(24)	0.05	$0.3 \cdot 10^{-3}$	0.037
	0_2^+	2_1^+	[4.8, 0.8]	4.06	0.6	1.76
	2_2^+	0_2^+	0.31(15)	0.3	0.26	0.15
	2_2^+	2_1^+	0.80(24)	0.6	0.015	0.59
	4_1^+	2_2^+	1.2(3)	0.25	0.015	0.05
^{184}Hg			$B(E2; I_i \to I_f)$ $[e^2\mathrm{b}^2]$			
	2_1^+	0_1^+	0.320(15)	0.39	1.31	1.02
	4_1^+	2_1^+	1.22(4)	1.09	2.37	1.82
	6_1^+	4_1^+	$1.92(9)^b$	1.8	2.74	2.27
	8_1^+	6_1^+	$1.92(8)^b$	1.9	3.05	3.76
	2_2^+	0_1^+	0.024(2)	0.021	0.018	0.034
	0_2^+	2_1^+	$1.3^{+0.7}_{-0.5}$	2.25	1.52	1.17
	2_2^+	0_2^+	$0.17^{+0.07}_{-0.09}$	0.49	0.3	0.19
	2_2^+	2_1^+	$0.54^{+0.09}_{-0.10}$	0.83	0.78	0.53
	4_1^+	2_2^+	[1, 0]	0.49	0.01	0.025
^{186}Hg			$B(E2; I_i \to I_f)$ $[e^2\mathrm{b}^2]$			
	2_1^+	0_1^+	$0.31^{+0.05}_{-0.04}$	0.28	0.29	0.97
	4_1^+	2_1^+	1.28(15)	0.40	2.00	1.68
	6_1^+	4_1^+	$1.46(6)^b$	1.84	2.37	2.10
	8_1^+	6_1^+	$1.27(9)^b$	1.97	2.62	2.42
	10_1^+	8_1^+	$1.50(16)^b$	1.99	2.88	2.70
	2_2^+	0_1^+	$0.5(2) \cdot 10^{-3}$	0.004	0.23	0.03
	2_2^+	0_2^+	≥ 1.7	0.97	0.22	0.21
	4_1^+	2_2^+	$3.1^{+1.5}_{-0.6}$	1.22	0.04	0.02
^{188}Hg			$B(E2; I_i \to I_f)$ $[e^2\mathrm{b}^2]$			$/Q_s$ [eb]
	2_1^+	0_1^+	0.34(5)	0.34	0.38	0.78
	4_1^+	2_1^+	0.48(4)	0.47	0.72	1.39
	2_2^+	0_1^+	$2.9(8) \cdot 10^{-4\,c}$	0.005	0.006	0.006
	2_2^+	2_1^+	$4.1(14) \cdot 10^{-3\,c}$	0.18	0.15	0.99
	2_1^+	2_1^+	$0.76^{+0.45}_{-0.30}$	0.58	1.26	-1.08

Good reproduction of the experimental data can be noticed when comparing to the results of the IBM-CM model. Note that in the IBM-CM approach seven parameters per isotope, plus two other parameters (the latter two fixed for the whole isotopic chain) were obtained through a least-squares fit to the available experimental information. In order to extract the IBM parameters the measured energies up to the 8_1^+ level, including the yrast and the non-yrast 0_2^+, $2_{1,2,3,4}^+$, $4_{1,2,3}^+$, $6_{1,2}^+$ and $3_{1,2}^+$ states, jointly with known measured $B(E2)$ values involving these states, were used. For the case of ^{182,184,186}Hg the experimental $B(E2)$ values between 2_2^+ and 2_1^+, $0_{1,2}^+$ and 4_1^+, as well as $B(E2; 10_1^+ \rightarrow 8_1^+)$, were not included in the fit of the IBM parameters (for more details see ref. [22], sects. III B and III C, tables I and III therein). In this respect, it can be expected that the IBM-CM model reproduces the experimental data better as compared to the BMF and GBH, for which no parameters are fitted to the properties of the Hg nuclei. A geometric interpretation of the IBM-CM can be obtained using the intrinsic state formalism. This provides a way to extract the mean-field energy corresponding to the IBM-CM Hamiltonian. Moreover, quadrupole deformation variables β and γ could be extracted for the Hg nuclei from the quadratic and cubic quadrupole invariants (see ref. [22], sects. V.B and V.C for a more detailed description). A good agreement between the IBM-CM model calculations and the experimental results supports the description of the nuclear structure in the mercury isotopes as resulting from two coexisting configurations characterized by different deformations. An alternative procedure to extract the IBM-CM parameters can be used, in which the parameters are derived starting from a self-consistent mean-field calculation. This has been realised by Nomura *et al.*, using the Gogny D1M force (see refs. [53,54] and references therein for a detailed description of the method used, as well as its application to the Hg nuclei).

6.3 Comparison to the two-state mixing calculations

As reported in ref. [20], the electromagnetic properties of even-even neutron-deficient mercury isotopes can be described in terms of mixing of two structures, which coexist at low-excitation energy. Matrix elements as well as signs of their products (interference terms), extracted from Coulomb-excitation measurements, can be compared to those resulting from the two-state mixing model. Within this phenomenological approach, following the notation introduced in ref. [55] and elaborated in ref. [56], the observed physical states can be written as linear combinations of two unmixed structures —structure I and structure II— with specific mixing amplitudes. The latter, taken from ref. [19], were derived from the fit of the known higher-lying level energies in the rotational bands, built upon the first two 0^+ states, using the variable moment of inertia model [57]. States with spin $I > 4$ are weakly mixed and manifest a rotational-like character, whereas a stronger mixing was deduced for states with spin $I = 2$, reaching the maximum of mixing for ^{184}Hg.

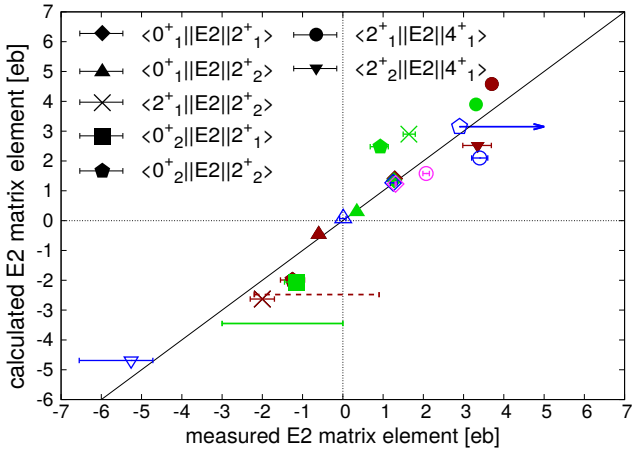

Fig. 16. (Color online) Transitional $E2$ matrix elements obtained in this work, compared to those extracted from the two-state mixing calculations for ^{182}Hg (full red), ^{184}Hg (full green), ^{186}Hg (open blue) and ^{188}Hg (open magenta). The results obtained for the $\langle 4_1^+ \| E2 \| 2_2^+ \rangle$ matrix element in ^{184}Hg and for the $\langle 0_2^+ \| E2 \| 2_1^+ \rangle$ matrix element in ^{182}Hg are marked with the solid green and dashed red horizontal lines, respectively.

For $^{182-188}$Hg the Coulomb-excitation data could be well reproduced by mixing between less-deformed oblate-like and more deformed prolate-like configurations [20], with their quadrupole properties assumed to be constant for the four isotopes considered. In fig. 16 a comparison between the experimental matrix elements and those resulting from the two-state mixing model is shown.

This figure is analogous to that presented in ref. [20] however, it contains the re-evaluated matrix elements for ^{182}Hg and ^{184}Hg. Experimental results, *i.e.*, magnitudes of matrix elements and signs of their products, are well reproduced by the two-state mixing model. Moreover, a significantly better agreement between the experimentally determined $\langle 2_1^+ \| E2 \| 0_2^+ \rangle$ and $\langle 4_1^+ \| E2 \| 2_2^+ \rangle$ matrix elements and those calculated within the two-state mixing model is now obtained for ^{184}Hg as compared to the results presented in ref. [20]. This is directly related to the experimentally extracted signs of the interference terms: $\langle 2_1^+ \| E2 \| 4_1^+ \rangle \langle 4_1^+ \| E2 \| 2_2^+ \rangle \langle 2_2^+ \| E2 \| 2_1^+ \rangle$ and $\langle 2_1^+ \| E2 \| 0_2^+ \rangle \langle 0_2^+ \| E2 \| 2_2^+ \rangle \langle 2_2^+ \| E2 \| 2_1^+ \rangle$, which are both negative in ^{184}Hg. The signs of these terms are opposite to those published in ref. [20].

The unperturbed quadrupole moments of the two 2^+ states, $Q_s(2^+)^{\mathrm{TSM}}$, belonging to two different unmixed configurations, were deduced from the experimental $\langle 2_2^+ \| E2 \| 2_1^+ \rangle$ matrix elements extracted for the mercury isotopes using the two-state mixing model (TSM). This yielded values of quadrupole moments for the pure 2^+ states equal to $136\, e\,\mathrm{fm}^2$ and $-303\, e\,\mathrm{fm}^2$ [20]. A comparison of the spectroscopic quadrupole moments (Q_s) for the 2_1^+ and 2_2^+ states in ^{182,184,186,188}Hg is shown in fig. 17. These Q_s values are calculated with the BMF, IBM-CM and GBH models and presented together with the unmixed values: the $Q_s(2^+)^{\mathrm{TSM}}$ ones and those obtained with the IBM-CM model, $Q_s(2^+)^{\mathrm{IBM}}_{\mathrm{pure}}$. The latter corre-

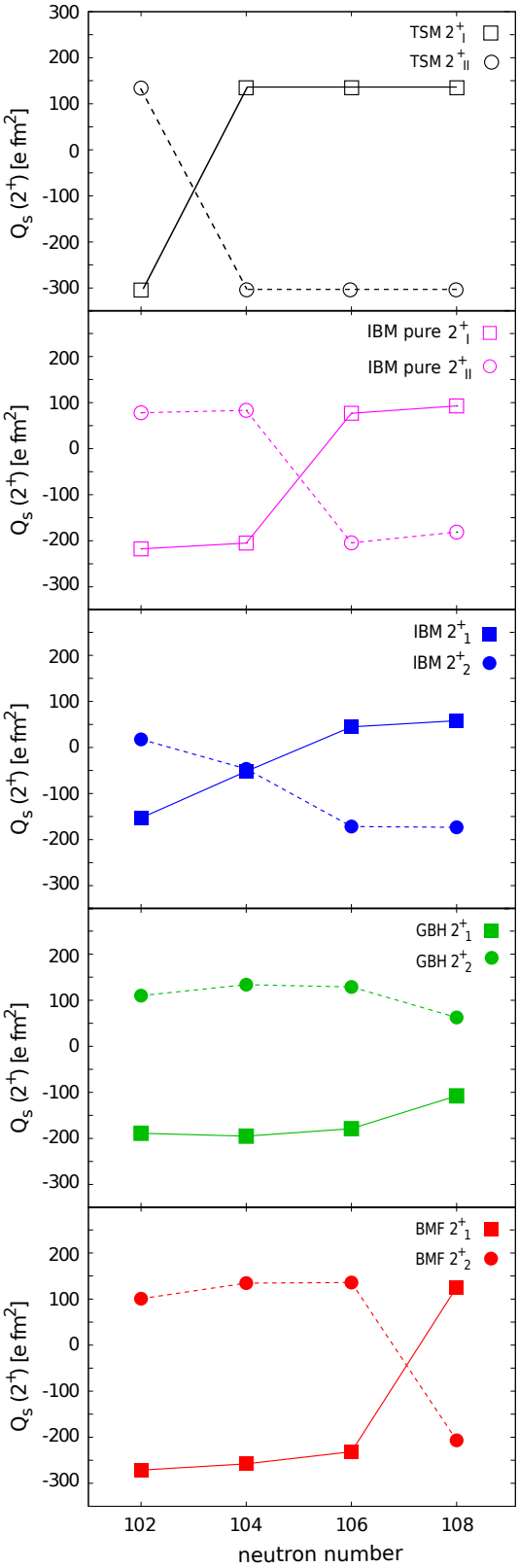

Fig. 17. (Color online) Spectroscopic quadrupole moments of the 2_1^+ (full squares) and 2_2^+ (full circles) states resulting from the IBM-CM (blue), GBH (green) and BMF (red) calculations. The unperturbed quadrupole moments from the IBM-CM [22] and two-state mixing (TSM) model are marked with the magenta and black open symbols, respectively.

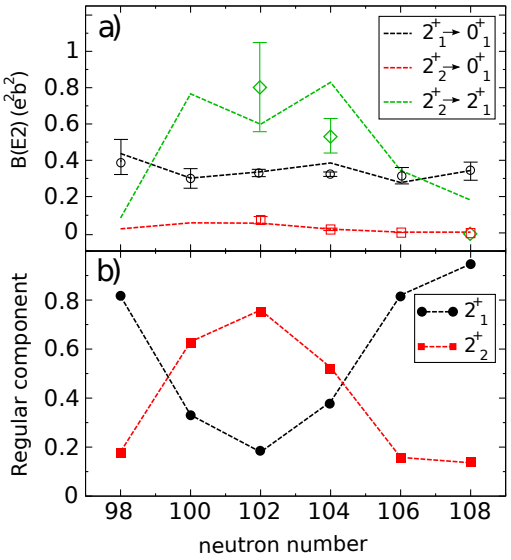

Fig. 18. (Color online) (a) Comparison of the experimental reduced transition probabilities (open symbols) and the IBM-CM results (dashed lines) involving the 2_1^+ and 2_2^+ states. Experimental values are taken from table 8 and from ref. [58] for ^{178}Hg and ref. [59] for ^{180}Hg; (b) IBM-CM results for the regular content (part of the wave function without particle-hole excitations) of the 2_1^+ and 2_2^+ states.

spond to the same Hamiltonian as the one used to obtain the results shown in fig. 15, column IBM-CM, but removing the interaction term acting between the $2h-0p$ and $4h-2p$ proton configurations.

The BMF calculations coherently predict that the dominantly prolate configuration is the lowest in energy up to $N=106$. A crossing between oblate and prolate configurations, corresponding to the positive and negative values of the quadrupole moments, respectively, takes place between $N=106$ and $N=108$. For the IBM-CM this transition happens at $N=104$, while no change of the structure of the 2^+ states is observed for the GBH. In the two-state mixing model the unperturbed values of Q_s are assumed to be the same for all four mercury isotopes. This assumption is consistent with the IBM-CM calculations, predicting indeed almost constant values of unperturbed Q_s (see fig. 17). The same constant trend for the calculated Q_s values also appears for the BMF and GBH calculations. The calculated Q_s values of the oblate 2^+ states coincide with the pure ones from the two-state mixing model, while the absolute value for the prolate 2^+ states is underestimated in BMF and GBH.

To summarize, though the excitation energy of the 2_1^+ state and the energy difference $E(2_2^+)-E(2_1^+)$ are almost constant for even-even $^{180-188}$Hg (as seen in the energy systematics in refs. [13, 14]), and the same is true for the $B(E2;2_1^+\rightarrow 0_1^+)$ and $B(E2;2_2^+\rightarrow 0_1^+)$ values as depicted in fig. 18(a), the underlying nuclear structure undergoes a dramatic change. As shown in the evolution of the IBM-CM wave functions in fig. 18(b), the composition of the 2_1^+ states changes from a rather pure structure-I character (the so-called regular configuration) for ^{186,188}Hg to a state dominated by structure II (the

intruder configuration) in ^{182}Hg. This substantial change in nuclear structure is also supported by the evolution of the IBM-CM Q_s values presented in fig. 17 or that of the theoretical and experimental $B(E2; 2_2^+ \rightarrow 2_1^+)$ values, as demonstrated in fig. 18(a). In conclusion, similar energies of states in an isotopic chain and similar transition probabilities do not always reveal a similar structure —the underlying mixing configuration can be somehow *concealed* as stated in refs. [22], [20] and [19].

7 Monopole transition strength

The large total conversion coefficients for the $2_2^+ \rightarrow 2_1^+$ transition in ^{182,184}Hg are a significant indicator of a strong mixing between the configurations having different shapes [60]. Combining the extracted $B(E2; 2_2^+ \rightarrow 2_1^+)$ values from the Coulomb-excitation experiment with a measured total conversion coefficients $\alpha_{tot}(2_2^+ \rightarrow 2_1^+)$ [17], the $E0$ transition strengths can be determined for ^{182}Hg and ^{184}Hg.

Following ref. [61] the $E0$ monopole strength $\rho^2(E0)$ for a $2_2^+ \rightarrow 2_1^+$ transition can be obtained from the expression

$$\rho^2(E0) = q_K^2 \left(\frac{E0}{E2}\right) \times \frac{\alpha_K(E2)}{\Omega_K(E0)} \cdot W_\gamma^{2_2^+ \rightarrow 2_1^+}(E2). \qquad (8)$$

The $q_K^2(\frac{E0}{E2})$ term is the intensity ratio of $E0$ and $E2$ K-conversion-electron components of the $2_2^+ \rightarrow 2_1^+$ transition. This ratio can be expressed by the total conversion coefficients and the $\delta(E2/M1)$ multipole mixing ratio for the $2_2^+ \rightarrow 2_1^+$ transition as follows:

$$q_K^2 \left(\frac{E0}{E2}\right) = \frac{I_K(E0)}{I_K(E2)} = \frac{(\alpha_{tot}^{E2+M1+E0} \cdot (1+\delta^2) - \alpha_{tot}^{E2} \cdot \delta^2 - \alpha_{tot}^{M1})}{\alpha_K^{E2} \cdot \delta^2} \cdot \frac{\Omega_K(E0)}{\Omega_{TOT}(E0)}. \qquad (9)$$

The Ω_K and Ω_{TOT} are electronic factors [62]. The $E2$-transition rate $W_\gamma^{2_2^+ \rightarrow 2_1^+}(E2)$ can be calculated directly from the $B(E2; 2_2^+ \rightarrow 2_1^+)$ value inferred from the Coulomb-excitation measurements quoted in table 8

$$W_\gamma^{2_2^+ \rightarrow 2_1^+}(E2) = \frac{8\pi}{\hbar} \frac{\lambda+1}{\lambda\left((2\lambda+1)!!\right)^2} \left(\frac{E_\gamma}{\hbar c}\right)^{2\lambda+1} \cdot B(E2; 2_1^+ \rightarrow 2_2^+) \qquad (10)$$

where the multipole order $\lambda = 2$.

Combining eqs. (8), (9), (10) and taking the total conversion coefficient $\alpha_{tot}(2_2^+ \rightarrow 2_1^+)$ equal to 7.2(13) and 14.2(36) for ^{182}Hg and ^{184}Hg, respectively [17], the resulting $E0$ monopole transition strength $\rho^2(E0) \cdot 10^3$ is 141(51) and 90(30) for ^{182}Hg and ^{184}Hg, respectively. The experimentally determined monopole strength depends on the $E2/M1$ mixing. As the latter is unknown, the value of $\delta(\frac{E2}{M1}) = 1.85$ was adopted, as described in sect. 5.1. Varying the $E2/M1$ mixing coefficient over a wide range of values, yielded $E0$ strengths consistent within error bars (*e.g.*, for ^{184}Hg: $\rho^2(E0) \cdot 10^3 = 101(34)$ corresponds to $\delta = 1$, $\rho^2(E0) \cdot 10^3 = 94(30)$ to $\delta = 5$ and $\rho^2(E0) \cdot 10^3 = 110(37)$ to $\delta = 0.5$). It is worth noting that the $E0$ monopole strength in ^{186}Hg was also inferred through combined in-beam electron and γ-ray spectroscopy, yielding a value of $\rho^2(E0) \cdot 10^3 = 60(50)$ [18].

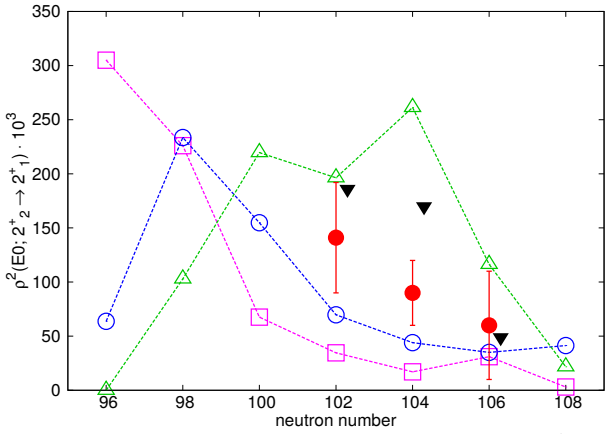

Fig. 19. (Color online) Monopole strength for the $2_2^+ \rightarrow 2_1^+$ transition resulting from the BMF (magenta open squares), GBH (blue open circles), IBM-CM (green open triangles) and the two-state mixing calculations (black full triangles) compared with the experimental values inferred for ^{182,184}Hg from this work and for ^{186}Hg taken from ref. [18] (red full circles).

Large $\rho^2(E0)$ values can be associated with strongly mixed states in nuclei that exhibit shape coexistence [60]. The transition strength can then be expressed as a function of the mixing amplitude (α) and the difference in the mean-square charge radii of the unperturbed configurations $\Delta\langle r^2\rangle$

$$\rho^2(E0) = \frac{Z^2}{R_0^4} \cdot \alpha^2(1-\alpha^2)\left[\Delta\langle r^2\rangle\right]^2, \qquad (11)$$

with Z being the proton number, $R_0 = r_0 A^{1/3}$, $r_0 = 1.2$ fm [60].

Mixing amplitudes for the 2^+ states in ^{182}Hg, ^{184}Hg and ^{186}Hg were taken from ref. [19] and are equal to 0.54, 0.72 and 0.95, respectively, for the regular configuration. We then assumed that the $\Delta\langle r^2\rangle$ value for the unperturbed 2^+ states is identical to that of the unperturbed 0^+ states. The latter is inferred from the large odd-even staggering in the isotope shifts in the mercury chain around $^{180-186}$Hg [4,6] following the procedure outlined in ref. [60]. The $\Delta\langle r^2\rangle$ was deduced to be equal to 0.55 fm^2 in ^{182}Hg, 0.48 fm^2 in ^{184}Hg and 0.44 fm^2 in ^{186}Hg. The resulting $\rho^2(E0) \cdot 10^3$ values are 186, 170 and 49 for ^{182}Hg, ^{184}Hg and ^{186}Hg, respectively.

In fig. 19, the $E0$ strengths of the $2_2^+ \rightarrow 2_1^+$ transition deduced from the experimental data are compared to the two-state mixing model predictions, the BMF model [16], the GBH model [52] and the IBM-CM model [63]. While the experimental value for ^{186}Hg is in agreement with all four calculations, the value for ^{182}Hg deviates from the predictions of both the BMF and GBH model calculations.

It is only consistent, within 1σ, with the two-state mixing approach and the IBM-CM model. For ^{184}Hg none of the calculations is in agreement with the experimental result. Both BMF and GBH models predict similar magnitudes of the $\rho^2(E0; 2_2^+ \rightarrow 2_1^+)$ especially around neutron mid-shell $N = 104$. Interesting to note is the rising trend of the BMF and GBH $E0$ strengths towards the lighter mercury isotopes, which is very different from the IBM-CM predictions. The IBM-CM calculations indicate that the largest values of the $\rho^2(E0; 2_2^+ \rightarrow 2_1^+)$ occur around neutron number $N = 104$. Both IBM-CM and GBH models predict a drop of the $\rho^2(E0)$ strengths for more neutron-deficient Hg isotopes (from $N = 98$ to $N = 96$). The origin of this behavior is currently not known.

8 Summary and outlook

Multi-step Coulomb-excitation experiments with postaccelerated radioactive ion beams of neutron-deficient, even-even ^{182,184,186,188}Hg isotopes were performed at the REX-ISOLDE facility at CERN. As a result, sets of $E2$ matrix elements were extracted between low-energy 0^+, 2^+ and 4^+ states populated in the experiments. The Coulomb-excitation data for ^{182,184}Hg were re-evaluated since new, revised spectroscopic information, $\alpha_{tot}(2_2^+ \rightarrow 2_1^+)$ and γ-ray branching ratios, have become available [17]. Complementary to our previous work [20], a systematic comparison of experimental results, *i.e.*, level energies and reduced quadrupole transition probabilities, with theoretical predictions, is shown. The results of calculations using the GBH and BMF models are, to a certain extent, in agreement with the experimental data. In the yrast bands of ^{182,184,186}Hg the experimental $B(E2)$ transition probabilities exhibit a very smooth behavior for states with spin $J \geq 4$, and this trend, as well as the absolute $B(E2)$ values, are fairly well reproduced by the GBH and BMF models. According to these models these states are of a prolate nature and lie lower in energy as compared to the oblate ones. A stronger mixing was deduced for states with $I = 2$, reaching a maximum for $N = 104$ [19]. For the low-lying 2^+ and 0^+ states the comparison with theory is less successful, partly due to the fact that the excitation energies of the different configurations are not correctly reproduced and their relative positions are reversed. In the case of the BMF calculations inclusion of the triaxial degree of freedom may be necessary in the description of the low-energy electromagnetic structure of the neutron mid-shell mercury isotopes.

Properties of the lowest-lying states of even-even $^{182-188}$Hg were also interpreted within a two-state mixing model. It is interesting to note how well the experimental results can be reproduced within this simple approach supporting the underlying assumption of two unperturbed different configurations that mix when states with equal spin and parity are close in energy. The results clearly show that the low-energy electromagnetic structure of $^{182-188}$Hg isotopes can be described in terms of mixing of two rotational configurations which coexist at low excitation energy. Mixing between a weakly deformed oblate-like band and a more deformed prolate-like band gains importance when going towards neutron midshell $N = 104$.

Because of the limited beam energy, only low-lying states could be studied at REX-ISOLDE. With the higher beam energy, up to 5 MeV/A, possible nowadays at HIE-ISOLDE, Coulomb excitation of neutron-deficient mercury isotopes can provide much richer information thanks to the higher multi-step excitation cross sections and increased sensitivity to the diagonal matrix elements. Thus our knowledge of higher-lying non-yrast states can be extended. Moreover, the quadrupole sum rules method can then be used to extract the shape invariants in a given state independently of the nuclear-structure models [64,65].

In order to draw firm conclusions from Coulomb-excitation experiments with exotic beams, complementary spectroscopic data are crucial [2]. Recently performed β/EC decay of neutron-deficient even-even Tl isotopes at HIE-ISOLDE intend to provide these data *i.e.*, precisely measure γ-ray branching ratios, conversion coefficients and mixing ratios for the low-lying (yrast and non-yrast) states in Hg isotopes [66]. Moreover, future Coulomb excitation experiments will also benefit from the use of the electron spectrometer SPEDE [67] which will provide direct information on intensities of conversion electrons, being of great importance for the nuclei in the $N = 104$ region [68].

Additional spectroscopic information for the higher-lying collective states can be obtained using unsafe Coulomb excitation. Beam energies available at HIE-ISOLDE up to 10 MeV/A will enable few-nucleon transfer reaction experiments to probe nuclear states in the light lead mass region. Furthermore, future Coulomb-excitation experiments of light odd-mass mercury isotopes aim to study the shape-coexisting isomers present in mercury nuclei. This, combined with one-neutron transfer reactions, will shed light on the underlying single-particle nature of these states. All these efforts open new possibilities to characterize shape coexistence in the mercury region [69].

The authors would like to thank the ISOLDE facility for providing excellent beams. This work was performed within the Polish-Belgian joint research project under the FWO-PAS agreement on scientific cooperation (FWO contract no. VS.084.16N). This work was supported by GOA/2010/010 (BOF KULeuven), by the IAP Belgian Science Policy (BriX network P6/23 and P7/12), by the European Commission within the 7th Framework Programme through I3-ENSAR (contract no. RII3-CT-2010-262010), by the National Science Centre, Poland, grant no. 2015/18/M/ST2/00523, by the U.K. Science and Technology Facilities Council grants PP/F000898/1, ST/FO12039/1, ST/J000094/1, ST/L005670/1 and ST/R004056/1 by the German BMBF under contracts No. 06DA9036I, 05P12RDCIA 06KY205I, 05P09PKCI5, 05P12PKFNE, 05P12WOFNF, 09MT9156, 05P15PKCIA and "Verbundprojekt 05P2015", Academy of Finland (Contract No. 131665), by the Spanish MINECO through FPA2015-65035-P project and the Spanish Project No. FIS2014-53448-C2-2, by the U.S. Department of Energy, Office of Science, Office of Nuclear Physics, under con-

tract No. DE-AC02-06CH11357. LP gratefully acknowledges support from the Polish National Science Center (NCN), grant no. 2013/10/M/ST2/00427. LPG acknowledges support from the FWO-Vlaanderen (Belgium) via an FWO Pegasus Marie Curie Fellowship. ACL gratefully acknowledges funding through ERC-STG-2014, grant agreement no. 637686.

Data Availability Statement This manuscript has no associated data or the data will not be deposited. [Authors' comment: All data generated during this study are contained in this published article.]

Publisher's Note The EPJ Publishers remain neutral with regard to jurisdictional claims in published maps and institutional affiliations.

References

1. K. Heyde, J.L. Wood, Rev. Mod. Phys. **83**, 1467 (2011).
2. K. Wrzosek-Lipska, L.P. Gaffney, J. Phys. G **43**, 024012 (2016).
3. J. Bonn, G. Huber, H.J. Kluge, L. Kugler, E.W. Ottenothers, Phys. Lett. B **38**, 308 (1972).
4. G. Ulm *et al.*, Z. Phys. A **325**, 247 (1986).
5. P. Dabkiewicz, F. Buchinger, H. Fischer, H.J. Kluge, H. Kremmling, T. Kuhl, A.C. Muller, H.A. Schuessler, Phys. Lett. B **82**, 199 (1979).
6. B. Marsh *et al.*, Nat. Phys. **14**, 1163 (2018).
7. D. Proetel, R.M. Diamond, F.S. Stephens, Phys. Lett. B **48**, 102 (1974).
8. N. Rud, D. Ward, H.R. Andrews, R.L. Graham, J.S. Geiger, Phys. Rev. Lett. **31**, 1421 (1973).
9. J.H. Hamilton *et al.*, Phys. Rev. Lett. **35**, 562 (1975).
10. J.D. Cole *et al.*, Phys. Rev. Lett. **37**, 1185 (1976).
11. W.C. Ma, A.V. Ramayya, J.H. Hamilton, S.J. Robinson, J.D. Cole, E.F. Zganjar, E.H. Spejewski, R. Bengtsson, W. Nazarewicz, J.Y. Zhang, Phys. Lett. B **167**, 277 (1986).
12. W.C. Ma, A.V. Ramayya, J.H. Hamilton, S.J. Robinson, M.E. Barclay, K. Zhao, J.D. Cole, E.F. Zganjar, E.H. Spejewski, Phys. Lett. B **139**, 276 (1984).
13. R. Julin, K. Helariutta, M. Muikku, J. Phys. G **27**, R109 (2001).
14. J. Elseviers *et al.*, Phys. Rev. C. **84**, 034307 (2011).
15. M. Bender, P.H. Heenen, P.G. Reinhard, Rev. Mod. Phys. **75**, 121 (2003).
16. J.M. Yao, M. Bender, P.H. Heenen, Phys. Rev. C **87**, 034322 (2013).
17. E. Rapisarda *et al.*, J. Phys. G: Nucl. Part. Phys. **44**, 074001 (2017).
18. M. Scheck *et al.*, Phys. Rev. C **83**, 037303 (2011).
19. L.P. Gaffney *et al.*, Phys. Rev. C **89**, 024307 (2014).
20. N. Bree *et al.*, Phys. Rev. Lett. **112**, 162701 (2014).
21. L. Próchniak, G. Rohoziński, J. Phys. G: Nucl. Part. Phys. **36**, 123101 (2009).
22. J.E. García-Ramos, K. Heyde, Phys. Rev. C **89**, 014306 (2014).
23. O. Kester *et al.*, Nucl. Instrum. Methods Phys. Res. B **204**, 20 (2003).
24. N. Warr *et al.*, Eur. Phys. J. A **49**, 40 (2013).
25. A.N. Ostrowski, S. Cherubini, T. Davinson, D. Groombridge, A.M. Laird, A. Musumarra, A. Ninane, A. di Pietro, A.C. Shotter, P.J. Woods, Nucl. Instrum. Methods A **480**, 448 (2002).
26. D. Cline, Bull Am. Phys. Soc. **14**, 726 (1969).
27. N. Bree *et al.*, Nucl. Instrum. Methods B **360**, 97 (2015).
28. T. Kibédi, T.W. Burrows, M.B. Trzhaskovskaya, P.M. Davidson, C.W. Nestor, Nucl. Instrum. Methods Phys. Res. Sect. A **589**, 202 (2008).
29. N. Bree, *Shape Coexistence in the Neutron-Deficient Mercury Isotopes Studied Through Coulomb Excitation* PhD Thesis (KU Leuven, Belgium, 2014).
30. R.B. Firestone, V.S. Shirley, C.M. Baglin, S.Y. Frank Chu, J. Zipkin, *Table of Isotopes*, 8th edition (John Wiley & Sons Inc., 1996).
31. J.H. Hubbell, P.N. Trehan, N. Singh, B. Chand, D. Mehta, M.L. Garg, R.R. Garg, S. Singh, S. Puri, J. Phys. Chem. Ref. Data. **23**, 339 (1994).
32. C.M. Baglin, Nucl. Data. Sheets **99**, 1 (2003).
33. T. Czosnyka, D. Cline, C.Y. Wu, Bull. Am. Phys. Soc. **28**, 745 (1983).
34. GOSIA User's Manual, `http://slcj.uw.edu.pl/en/gosia-code/`.
35. J.D. Cole *et al.*, Phys. Rev. C **16**, 2010 (1977).
36. R. Béraud, M. Meyer, M.G. Desthuilliers, C. Bourgeois, P. Kilcher, J. Letessier, Nucl. Phys. A **284**, 221 (1977).
37. J.D. Cole *et al.*, Phys. Rev. C **30**, 1267 (1984).
38. T. Grahn *et al.*, Phys. Rev. C **80**, 014324 (2009).
39. M. Scheck *et al.*, Phys. Rev. C **81**, 014310 (2010).
40. P.K. Joshi *et al.*, Int. J. Mod. Phys. E **3**, 757 (1994).
41. M. Zielińska, L.P. Gaffney, K. Wrzosek-Lipska, E. Clément, T. Grahn, N. Kesteloot, P. Napiorkowski, J. Pakarinen, P. Van Duppen, N. Warr, Eur. Phys. J. A **52**, 99 (2016).
42. J. Pakarinen *et al.*, J. Phys. G **44**, 064009 (2017).
43. E. Clément *et al.*, Phys. Rev. C **94**, 054326 (2016).
44. N. Kesteloot *et al.*, Phys. Rev. C **92**, 054301 (2015).
45. K. Wrzosek-Lipska *et al.*, Phys. Rev. C **86**, 064305 (2012).
46. N. Bijnens *et al.*, Phys. Rev. C **58**, 754 (1998).
47. M. Bender, K. Rutz, P.G. Reinhard, J.A. Maruhn, Eur. Phys. J. A **7**, 467 (2000).
48. F. Iachello, A. Arima, *The Interacting Boson Model* (Cambridge University Press, Cambridge, UK, 1987).
49. P.D. Duval, B.R. Barrett, Phys. Lett. B **100**, 223 (1981).
50. P.D. Duval, B.R. Barrett, Nucl. Phys. A **376**, 213 (1982).
51. B. Singh, Nucl. Data Sheets **95**, 387 (2002).
52. L. Próchniak, private communication.
53. K. Nomura, R. Rodríguez-Guzmán, L.M. Robledo, Phys. Rev. C **87**, 064313 (2013).
54. K. Nomura, T. Otsuka, P. Van Isacker, J. Phys. G **43**, 024008 (2016).
55. P. Van Duppen, M. Huyse, J.L. Wood, J. Phys. G **16**, 441 (1990).
56. N. Kesteloot, *Deformation and Mixing of Co-Existing Shapes in the Neutron-Deficient Polonium Isotopes* PhD Thesis (KU Leuven, Belgium, 2015).
57. M.A.J. Mariscotti, G. Scharff-Goldhaber, B. Buck, Phys. Rev. **178**, 1864 (1969).

58. C. Mueller-Gatermann *et al.*, Phys. Rev. C **99**, 054325 (2019).
59. E.A. Mccutchan, Nucl. Data Sheets **126**, 151 (2015).
60. J.L. Wood, E.F. Zganjar, C.D. Coster, K. Heyde, Nucl. Phys. A **651**, 323 (1999).
61. T. Kibédi, R.H. Spear, At. Data Nucl. Data Tables **89**, 77 (2005).
62. E.L. Church, J. Weneser, Phys. Rev. **103**, 1035 (1956).
63. J.E. García-Ramos, K. Heyde, private communication.
64. K. Kumar, Phys. Rev. Lett. **28**, 249 (1972).
65. D. Cline, Annu. Rev. Nucl. Part. Sci. **36**, 683 (1986).
66. K. Rezynkina *et al.*, CERN-INTC 079 P-511 (2017).
67. P. Papadakis *et al.*, Eur. Phys. J. A **54**, 42 (2018).
68. K. Wrzosek-Lipska *et al.*, CERN-INTC 063 P-364 (2012).
69. P. Van Duppen *et al.*, CERN-INTC 044 I-110 (2010).